Nano Research

Open Access

Review Article

Atomic-level magnetism modulation of nanocrystals for biomedical imaging

Yuehao Gan[1,3], Hui Du[1], Qiyue Wang[1,3], Fangyuan Li[2,3] ✉, and Daishun Ling[1,3] ✉

[1] *Frontiers Science Center for Transformative Molecules, School of Chemistry and Chemical Engineering, School of Biomedical Engineering, National Center for Translational Medicine, State Key Laboratory of Oncogenes and Related Genes, Shanghai Jiao Tong University, Shanghai 200240, China*
[2] *Department of Clinical Laboratory, Songjiang Research Institute, Shanghai Key Laboratory of Emotions and Affective Disorders (LEAD), Songjiang Hospital Affiliated to Shanghai Jiao Tong University School of Medicine, Shanghai 201600, China*
[3] *World Laureates Association (WLA) Laboratories, Shanghai 201203, China*

Cite this article: *Nano Research*, **2025**, *18*, 94907251. https://doi.org/10.26599/NR.2025.94907251

ABSTRACT: Structural regulation of magnetic nanomaterials has been pivotal for enhancing their magnetic properties and improving their performance in biomedical imaging. While numerous studies have focused on mesoscopic tuning of these nanocrystals, the desired level of precision has not been consistently achieved. The advent of atomic-level manipulation of nanostructures presents a sophisticated approach to the precise modulation of magnetism. However, a comprehensive understanding of how to modulate magnetism at the atomic level has remained elusive, impeding the advancement of this technique. This review aims to bridge this gap by conducting a thorough examination of the application of atomic-level techniques in magnetically modulating nanocrystals for biomedical imaging. It will synthesize current knowledge, elucidate the fundamental principles of atomic-level magnetic modulation, and highlight the contemporary biomedical imaging applications of these nanocrystals. The review will also discuss the challenges currently encountered and provide insights into emerging trends, suggesting potential directions for future research, thereby guiding the development of this rapidly evolving field.

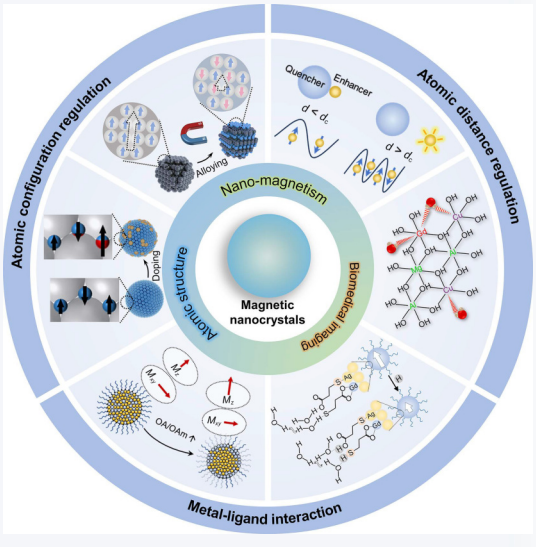

KEYWORDS: atomic structure, magnetism modulation, magnetic nanocrystals, biomedical imaging

1 Introduction

Structure is universally recognized as the fundamental characteristic that determines the properties of matter. Through precise control of structural parameters at different scales, remarkable progress has been achieved in the advancement of high-performance materials, evident in both research and industrial settings [1–4]. In the domain of nanoscale materials, key attributes such as particle size, shape, and crystalline structure are pivotal in dictating the optical, thermoelectric, and magnetic properties of inorganic nanocrystals [5–9]. These characteristics have proven invaluable in improving performance across a spectrum of fields, including energy, catalysis, and nanomedicine [10–12].

As a quintessential example, the precise manipulation of the structure of magnetic nanocrystals has been strategically utilized to fine-tune their magnetic properties, which in turn enhances the sensitivity and specificity of biomedical imaging techniques [13–18]. Core magnetic properties such as magnetization, coercivity, and magnetic anisotropy are crucial for correlating nanostructure design with the efficacy of biomedical imaging [19–21]. There has been a significant investment of research efforts in elucidating the mechanisms that dictate the interplay between structural attributes and magnetic behavior of nanocrystals, with the aim of optimizing their magnetic responses [22–26]. Despite the progress that has yielded relatively optimized nanoprobes and consequent enhancements in disease detection through imaging,

Received: September 30, 2024; **Revised:** November 11, 2024
Accepted: January 11, 2025

✉Address correspondence to Fangyuan Li, lfy@shsmu.edu.cn; Daishun Ling, dsling@sjtu.edu.cn

these methodologies still grapple with achieving the requisite precision and control in modulating the nanoarchitecture. For example, although extensive studies have focused on augmenting the T_1 relaxivities of ultrasmall iron oxide nanoparticles via size optimization, a definitive consensus on the underlying variation patterns or the optimal size remains elusive [15, 17, 27, 28]. This underscores the need for a more refined approach that provides exacting control over the directional modulation of magnetic properties, thereby facilitating the creation of more sophisticated and responsive magnetic nanocrystals for the advancement of biomedical imaging.

The coordinated alignment of atomic magnetic moments within a nanocrystal, driven by their complex interactions, results in the nanocrystal's macroscopic magnetic moment [29–31]. Achieving atomic-level precision in modulation allows researchers to control the spatial arrangement and chemical composition of atoms within these nanocrystals, thereby fine-tuning their magnetic properties [32–34]. For example, the doped inclusion of exogenous gadolinium ions, renowned for their substantial outmost unpaired electrons, into the lattice of ferrite nanocrystals in a site-selective manner, significantly enhances the overall net magnetic moment [35]. This enhancement leads to a decrease in coercive force and an enhancement in super-paramagnetism, thereby improving the nanocrystals' properties for biomedical applications. Beyond these internal atomic rearrangements, recent studies have also emphasized the importance of interatomic interaction between ligand and metal atoms [36–38]. Phenomena such as induced atomic segregation and the creation of permanent magnetic moments on the particle surface have a significant impact on the modulation of nanocrystals' magnetism. Despite these insights, the area of ligand-mediated atomic regulation remains in its infancy. The emerging methods of atomically precise magnetism modulation have attracted considerable attention and are increasingly being incorporated into the field of biomedical imaging [36, 37, 39, 40]. However, the literature lacks systematic reviews that explore these strategies in depth. This review aims to address this gap by providing a comprehensive analysis of how atomic-level techniques are applied in the magnetic modulation of nanocrystals for biomedical imaging. It will synthesize the current body of knowledge, clarify the foundational principles of representative atomic-level magnetic modulation, highlight the contemporary applications of these nanocrystals within biomedical imaging, and

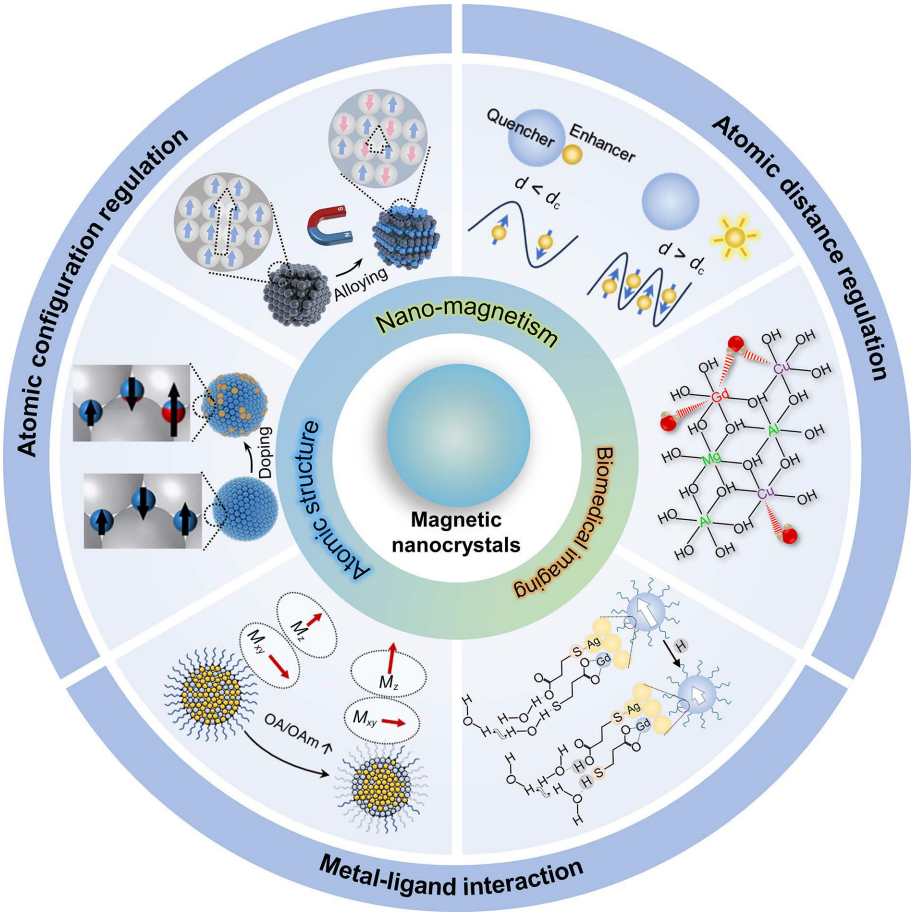

Figure 1 Schematic illustration of the major strategies of atomic-level magnetism modulation. Current strategies mainly involve metal alloying, metal ion doping, distance-dependent magnetic interactions, and metal-ligand interaction-mediated magnetism modulation. Parameters such as saturation magnetization (M_s), magnetic moment (μ_B), and coercivity can be finely tuned to meet biomedical imaging requirements. The inset images about ligand-induced atomically segregated alloy nanoprobe is reproduced with permission from Ref. [36], © American Chemical Society 2024. The inset images about ligand-mediated magnetism-conversion nanoprobe is reproduced with permission from Ref. [37], © Wiley-VCH GmbH 2024. The inset images about the magnetic resonance enhancement tuning (MRET) effect is reproduced with permission from Ref. [46], © Springer Nature Limited 2017. The inset images about adjacent effect of the proximal cation ions is reproduced with permission from Ref. [62], © The Royal Society of Chemistry 2023.

outline the existing challenges. Additionally, it will offer perspectives on emerging trends and potential directions for future research, thereby guiding the advancement of this dynamic field (Fig. 1).

2 Atomic-level magnetism modulation strategies

Principally, atomic-scale engineering of nanocrystals entails precise control over atomic arrangements the nanocrystal lattice, including lattice geometry, atomic positioning, and interatomic spacing [41–45]. In the realm of atomic-level magnetism modulation, recent research has predominantly concentrated on techniques such as atomic configuration regulation, atomic distance regulation and metal-ligand interaction, which are concretely applied as metal alloying and ion doping, distance-dependent magnetic interactions and metal-ligand interaction-mediated magnetism modulation [37, 46–49]. By employing these strategies, key magnetic parameters such as saturation magnetization (M_s), magnetic moment (μ_B), and coercivity can be precisely tuned to meet specific imaging requirements and improve the performance of nanocrystals in biomedical applications.

2.1 Metal alloying and metal ion doping

The crystalline structure of a nanocrystal is fundamental to its magnetic properties because it dictates the atomic and electronic environment in which the magnetic moments exist and interact. The structural factors, such as lattice geometry, symmetry, atomic arrangement, and so forth, shape the electronic environment and atomic interactions, thus affecting magnetization, susceptibility, and response to magnetic fields. Therefore, using atomic adjustment to govern crystalline structure is a direct and effectual strategy for modulating their magnetism, which mainly involves metal alloying and metal ions doping.

In recent years, the controlled synthesis of bimetallic nanoalloys combining noble with base metals has represented a promising approach for tailoring the magnetic properties and elemental distribution within these particles [23, 50, 51]. For example, nanoalloys, such as FePt and FeCo, typically exhibit higher magnetic moments compared to conventional ferromagnetic nanocrystals. This enhancement is due to the exchange coupling interactions that align their magnetic spins in parallel to the external magnetic field, thereby increasing their overall magnetic response. When compared with iron oxide nanoparticles, FeCo-based nanocrystals displayed nearly a 2 times higher magnetic moment (2.4 μ_B vs. ~ 1.3 μ_B) [52], which held good promise in enhancing signal intensity in magnetic imaging, particularly T_2-weighted (T_2-*W*) magnetic resonance imaging. Despite this, considering that the intensified T_2 decaying effect is always along with rapidly dephased longitudinal magnetization (M_z), magnetic nanoalloys with higher magnetic moments are detrimental to T_1 contrast enhancement. This puts forward demands to weaken the T_2-decaying effects while enhancing the recovery of M_z for T_1-Weighted (T_1-*W*) imaging. Given these, our group has recently reported antiferromagnetic FePt nanoprobes (AFNPs) for tailored ultrahigh-field (UHF) T_1 MR contrast enhancement, which present antiparallel magnetic moments compared with traditional paramagnetic nanoprobes (PMNPs), and thus have extremely small magnetization than that of PMNPs (Figs. 2(a)–2(d)) [53]. These contributed to a much lower T_2 relaxivity (r_2) and a better T_1 contrast enhancement under UHF (Figs. 2(e)–2(g)). Therefore, the rational design of alloyed magnetic nanocrystals with proper magnetic moments could selectively improve the T_1 or T_2 contrast ability for realizing high-resolution magnetic resonance imaging (MRI). In addition, doping with transition metal ions or rare earth metal ions represents another effective way of tuning internal crystalline structure and magnetic properties of nanocrystals [39, 40, 54–56]. In a typical magnetic iron oxide with spinel or inverse spinel structure, Fe^{2+} and Fe^{3+} ions are distributed in either octahedral (O_h) or tetrahedral (T_d) sites. In O_h sites, magnetic spins are aligned parallel, whereas in T_d sites, they are oriented antiparallel to an external magnetic field. Therefore, the net magnetic moment is the residual spin magnetic moment post the antiferromagnetic interaction. The doping of external metal ions alters the positions that metal cations occupy within the lattice, thereby leading to notable modifications to the number of unpaired outer electrons in the nanoparticles, the crystalline structure, and also the magnetic characteristics (including saturation magnetization, susceptibility, and magnetic moment, along with coercivity).

For example, Cheon and co-workers first proposed a transition metal doping strategy for increasing the T_2 relaxivity of ferrite nanoparticles by tuning their magnetic moment [57]. They fabricated a series of ferrite nanoparticles termed MFe_2O_4, where the external M^{2+} (M = Mn, Ni, and Co) was readily introduced to displace Fe^{2+}. The estimated magnetic moments per unit of $MnFe_2O_4$, Fe_3O_4, $CoFe_2O_4$, and $NiFe_2O_4$ were 5, 4, 3 and 2 μ_B, respectively, where the M_s value of these nanoparticles gradually decreased from 110 emu·g^{-1} for $MnFe_2O_4$ to 85 emu·g^{-1} for $NiFe_2O_4$. Therefore, the $MnFe_2O_4$ NPs displayed the highest T_2 relaxivity of 358 mM^{-1}·s^{-1}, which is 2 times higher than that of iron oxide NPs. Accordingly, compared to transition metal ions, rare earth metal ions, such as holmium ions (Ho^{3+}), dysprosium ions (Dy^{3+}), and gadolinium ions (Gd^{3+}), feature the largest number of outmost unpaired electrons, and thus have the potential to dramatically enhance the magnetic moment of ferrite NPs with lower doping content. For example, Wu and co-workers have synthesized a series of low-dose Gd^{3+} doped iron oxide nanoclusters with different Gd content [35]. The external Gd^{3+} ions tend to occupy the Fe^{3+} in the O_h site first, which thereby results in an increased net magnetic moment. When higher content of Gd^{3+} ions was introduced, some of them were inclined to replace the $Fe^{3+}T_d$, thus leading to a decreased net magnetic moment. Notably, to balance the energy increment of single-site doping, the Gd^{3+} ions replacement will occur in the two sites alternately with the increasing of Gd^{3+} ions content, thereby the net magnetic moment remains steady and fluctuating. These provided an effective approach to finely tune the Gd^{3+} ions content, reduce the coercive force, and obtain the best-performing T_2 magnetic resonance (MR) contrast agents. The final $Gd_{0.072}Fe_{2.928}O_4$ NCs have shown an extremely high r_2 value under 7.0 T MRI, approximately 4 times higher than that of pristine magnetic iron oxide NPs (MIONPs). Despite these advances, there are rarely research works focusing on the structural regulation by atomic doping for enhancing the T_1 contrast performance of nanoprobe, particularly under ultrahigh-field magnetic resonance imaging (UHF)-MRI, where the longitudinal relaxation of water proton is susceptible to strong T_2-decaying effect. To address this issue, our group has recently developed structural defect-enabled magnetic neutrality nanoprobes (MNNs) comprising ultrasmall zinc-doped ferrite ($Zn_xFe_{3-x}O_4$) nanoparticles for UHF-MRI [48]. On the one hand, the introduction of diamagnetic zinc atoms influences the magnitude and orientation of the magnetic moments within the nanoparticles. On the other hand, the increase in oxygen vacancies (OVs), induced by zinc doping, intensifies the internal

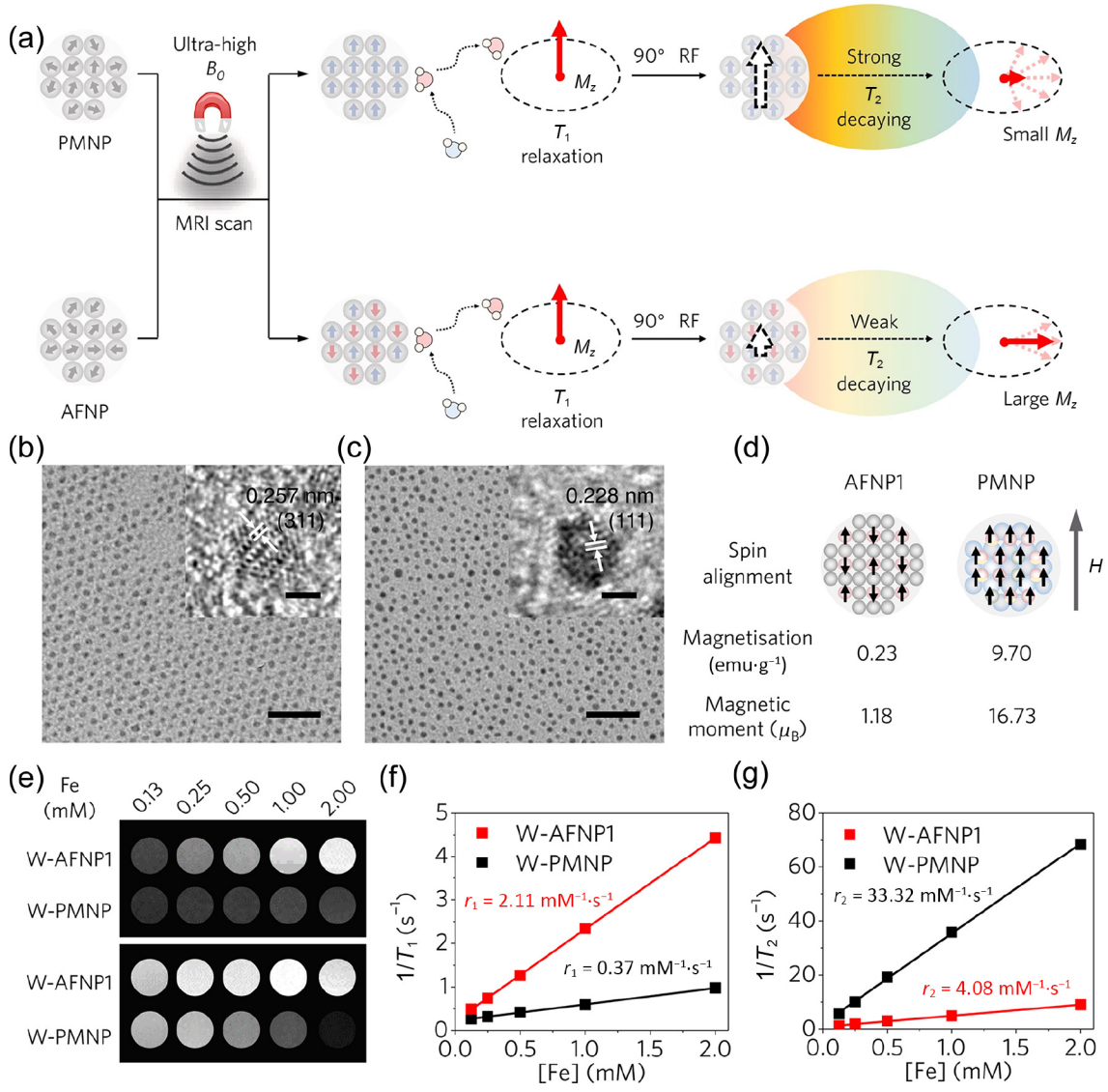

Figure 2 Metal alloying-mediated magnetism modulation of nanocrystals for biomedical imaging. (a) The imaging mechanism of PMNPs and AFNPs at UHF-MRI. Transmission electron microscopy (TEM) images of (b) PMNPs and (c) AFNPs, scale bars: 20 nm. (d) Schematic diagram of the spin directions of AFNPs and PMNPs at an external magnetic field, as well as the magnetic moments and magnetization. (e) T_1- and T_2-*W* images of AFNPs and PMNPs. (f) $1/T_1$ and (g) $1/T_2$ values of AFNPs and PMNPs. Reproduced with permission from Ref [53], © Liang, Z. et al. 2021.

spin-canting effect, which, in conjunction with the surface spin-canting effect, results in a notable decrease in magnetization (Figs. 3(a)–3(c)). Moreover, with the Zn content in $Zn_xFe_{3-x}O_4$ increasing, the longitudinal relaxivities (r_1) increased from ~ 0.36 to ~ 1.86 $mm^{-1}·s^{-1}$, while the transverse relaxivities (r_2) exhibited a gradual decrease from ~ 3.91 to ~ 1.96 $mm^{-1}·s^{-1}$ aligning with the trend in maximum magnetization (Fig. 3(d)). Meanwhile, the r_2/r_1 values displayed a significant drop (from ~ 10.96 to ~ 1.06) following the increase of Zn ratio (Fig. 3(e)). Conclusively, this synergistic effect induced by Zn doping presents a state of magnetic neutrality that minimizes the T_2-decay effect and enhances the T_1 contrast capability of the MNNs, making them highly sensitive to UHF-MRI (Fig. 3(f)).

2.2 Distance-dependent magnetic interactions

In addition to magnetism modulation through atomic hybridization within the crystalline structure, the distance-dependent magnetic interaction has been established as another potent method for adjusting magnetic properties. A prime example of this is the magnetic resonance enhancement tuning (MRET) effect. The MRET effect was first reported by Cheon and co-workers in 2016, which is a nanoscale distance-dependent T_1 MR phenomenon occurring between a superparamagnetic quencher and a paramagnetic enhancer [46, 58]. Unlike typical T_1 contrast agents featuring constant signal, an MRET nanoprobe is composed of a quencher-like superparamagnetic ferrite nanoparticle and a paramagnetic metal ion as an enhancer, both of which are linked by a specific chemical bond, where the T_1 MR signal state could be well controlled through the structural change of this nanoprobe. In principle, the action mechanism of T_1 contrast agents highly depends on the electron spin fluctuation-accelerated water proton relaxation, which then results in an enhanced T_1 MR signal. This process will take effect when the distance between the enhancer and the quencher is greater than a critical value (d_c), where the quencher can scarcely exert influence over the distant enhancer (Fig. 4(a)). As the enhancer and the quencher get closer to each other, the spin

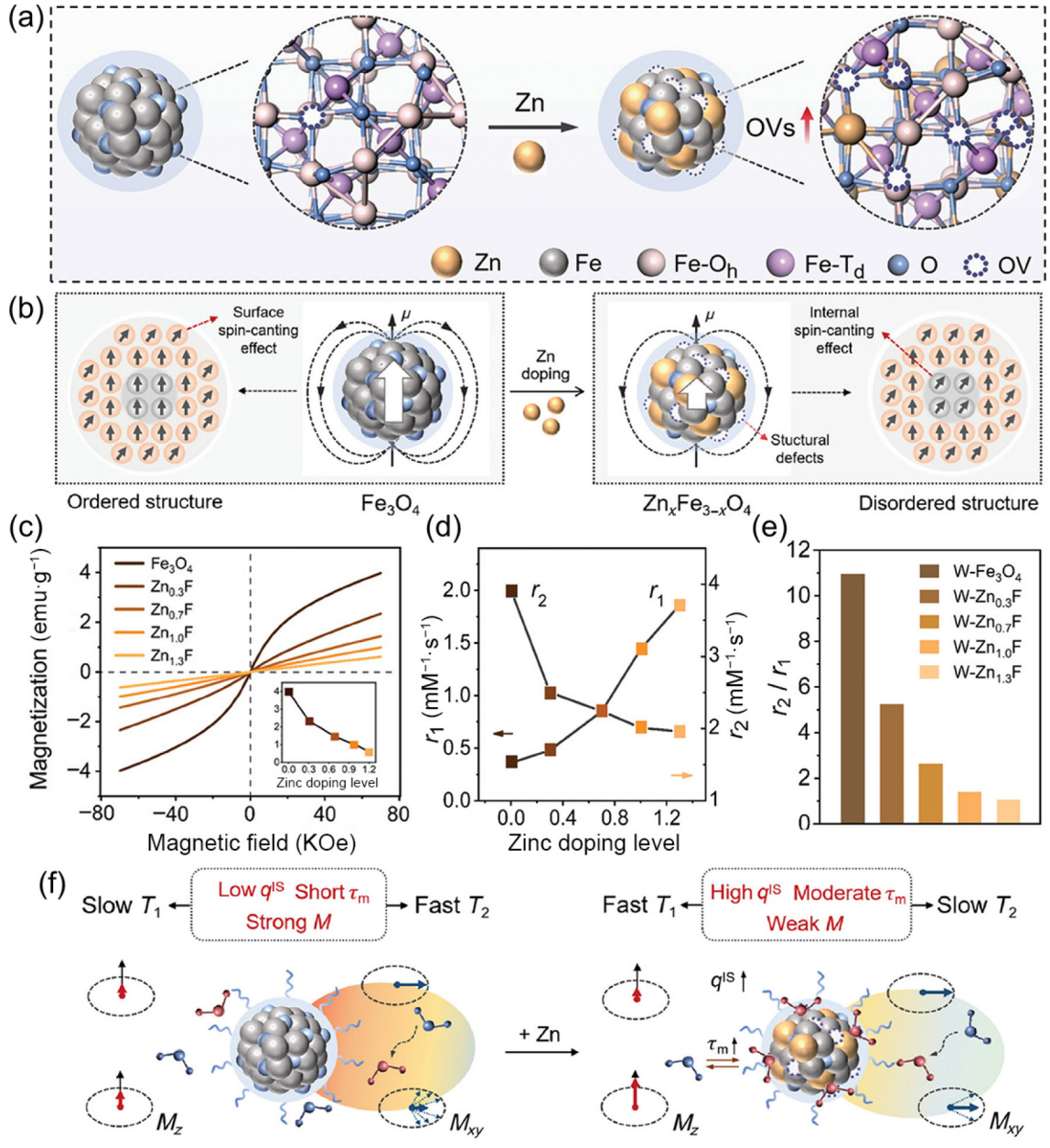

Figure 3 Metal ion doping-mediated magnetism modulation of nanocrystals for biomedical imaging. (a) Schematic illustration of OVs levels in the nanoprobe that regulated by precise stoichiometric control of zinc ions into the ferrite. (b) The UHF-MRI T_1 contrast enhancement mechanism of $Zn_xFe_{3-x}O_4$ MNPs. (c) Magnetization curves (M–H) of $Zn_xFe_{3-x}O_4$ MNPs at 300 K. The inset image shows the maximum magnetization of $Zn_xFe_{3-x}O_4$ MNPs at 7 T. (d) r_1, r_2 values and (e) r_2/r_1 values of W-$Zn_xFe_{3-x}O_4$ MNPs at 300 K. (f) The effect of changes in zinc atoms modulation-induced magnetic moment arrangement and spin-canting effects on the magnetic properties of $Zn_xFe_{3-x}O_4$ MNPs. Reproduced with permission from Ref. [48], © Wiley-VCH GmbH 2024.

fluctuation will be slowed and thus unable to accelerate the water proton relaxation. According to this mechanism, the key to controlling the MR signal state is the separation distance. In this pioneering work, Cheon and co-workers have initially synthesized a series of MRET probes comprising $Zn_{0.4}Fe_{2.6}O_4$ NPs and Gd-DOTA for proof of concept, where the silicon dioxide served as the separating layer to control the distance. It was found that as the separating distance decreased from 18 to 2 nm, the T_1 relaxivity of this MRET nanoprobe reduced from 1.58 to 0.13 $mM^{-1}·s^{-1}$ (Figs. 4(b) and 4(c)). Notably, when the practical distance was set to 7 nm, the T_1 MRI quenching efficiency was 50%, therefore this value was determined as d_c (Fig. 4(d)). Besides, by delicately designing nanoarchitecture with proper chemical or biologic linker bridging the enhancer and the quencher, numerous *in vivo* physiological or pathological biomarkers could be precisely sensed qualitatively and quantificationally with MRET probe-based molecular MR imaging technology through the responsive change of molecular conformation or breaking of chemical bond, which is crucial for understanding microscopic biological process and realizing high-sensitivity disease diagnosis [59, 60]. Based on this work, Li and co-workers have presented the development of a novel two-way magnetic resonance tuning (TMRET) nanotechnology for enhanced and non-invasive biological imaging [61]. This TMRET nanoprobe represents an innovative approach to enhancing MRI contrast through a distance-dependent interaction between a T_1 contrast agent (P-Mn) and a T_2 contrast agent (SPIO) encapsulated

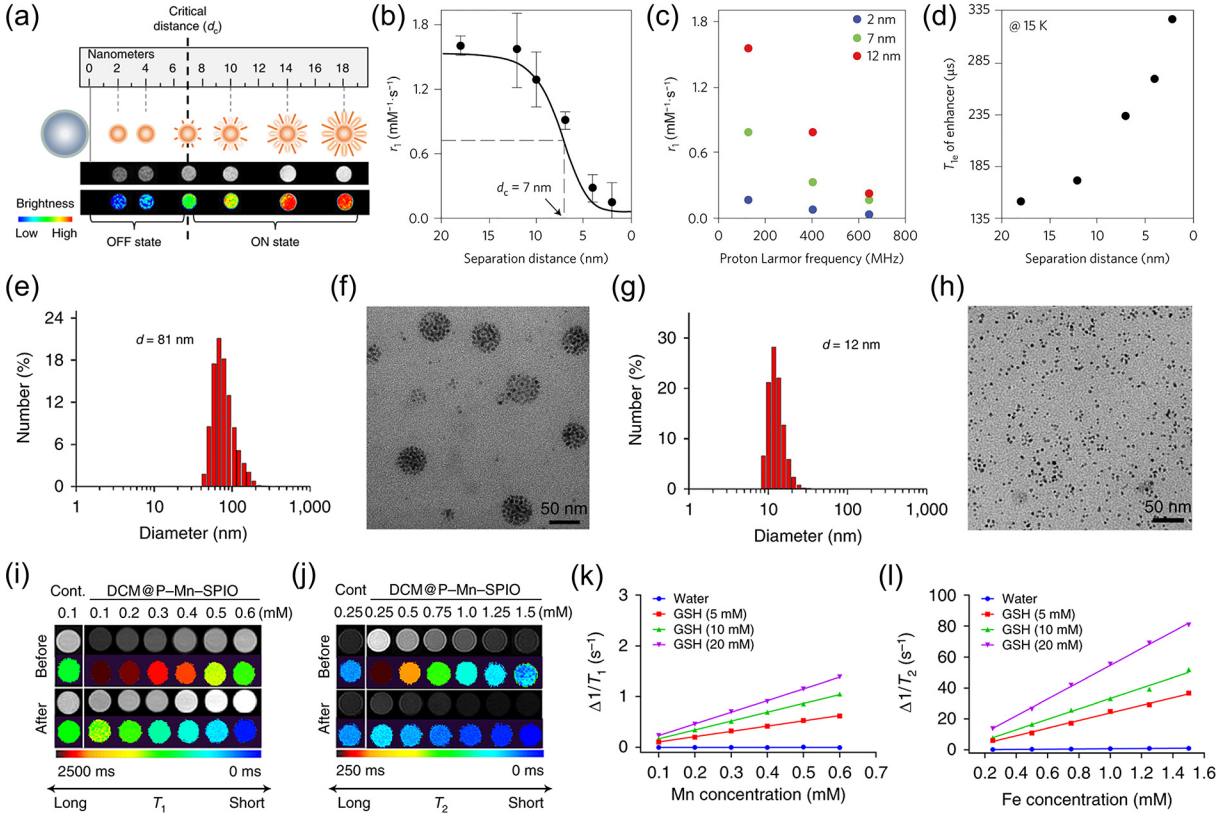

Figure 4 Distance-dependent magnetic interactions for biomedical imaging. (a) Schematic illustration of an MRET sensor. Reproduced with permission from Ref. [58], © Shin, T.-H. et al. under exclusive licence to Springer Nature Limited 2018. (b) A plot of the T_1 relaxivity coefficient (r_1) versus separation distance of MRET probe. (c) The r_1 values of the enhancer with a separation distance of 2 nm (blue), 7 nm (green) and 12 nm (red) at various proton Larmor frequencies of 128 MHz (3 T), 400 MHz (9.4 T) and 648 MHz (15.2 T). (d) A plot of T_{1e} versus the separation distance at 15 K. Decrease in the separation distance elongates T_{1e}. Reproduced with permission from Ref. [46], © Springer Nature Limited 2017. (e) Diameter distributions measured by dynamic light scattering and (f) TEM micrograph of DCM@P–Mn–SPIO. (g) Diameter distributions and (h) TEM micrograph of disassembled DCM@PMn–SPIO treated with 20 mM GSH and 3 mg·mL^{-1} sodium dodecyl sulfate (SDS) for 24 h. (i) T_1-W and the color-coded T_1 map and (j) T_2-W and the color-coded T_2 map of DCM@P–Mn–SPIO before and after the payload release (triggered by GSH). The changes in (k) $1/T_1$ values ($\Delta 1/T_1$) and (l) $1/T_2$ values ($\Delta 1/T_2$) of DCM@P–Mn–SPIO at different concentrations before and after incubation with GSH (0, 5, 10 and 20 mM) and SDS. Reproduced with permission from Ref. [61], © Wang, Z. et al. under exclusive licence to Springer Nature Limited 2020.

within the same micelle. In the initial state, the proximity of these agents leads to a "quenching" effect, reducing both T_1 and T_2 relaxation rates and thus the MRI signal. This interaction is governed by the magnetic fields of the agents, where the SPIO's strong magnetic field can slow the electron spin relaxation of the Mn^{2+} ions in P-Mn for T_1 quenching, and disrupt the magnetic environment for water protons in the case of T_2 quenching. However, the system is designed to be responsive to biological stimuli, such as the elevated levels of glutathione (GSH) found in tumor environments. Upon encountering such stimuli, the micelle disassembles, increasing the distance between the agents and reducing their magnetic interaction (Figs. 4(e)–4(h)). This leads to a recovery of the agents' normal relaxation properties, enhancing the MRI signal (Figs. 4(i)–4(l)). The TMRET system's ability to tune the MRI signal by controlling the distance between the agents allows for precise control over MRI contrast, enabling the development of smart contrast agents capable of high-resolution, functional imaging with minimal background noise, and providing a significant advancement in diagnostic imaging capabilities. In addition, incorporating two paramagnetic cations, particularly Gd^{3+} and Cu^{2+}, into a nanostructure emerges as an efficacious strategy for harnessing atomic-scale magnetic interactions [62]. The pioneering research by Xu and colleagues has unveiled that the proximity of these cations engenders a synergistic magnetic effect, namely an adjacent effect. This effect notably amplifies the relaxation rate of surrounding water protons, culminating in an enhanced T_1-W MRI signal.

2.3 Ligand-mediated magnetism modulation

Surface ligand plays an important role in the synthesis and application of nanocrystals [63–67]. Early practice on ligand engineering of biomedical nanoparticles mainly focused on shape controlling in synthetic processes, structure stabilizing for *in vivo* circulation, and functional targeting in therapy and diagnosis [68–71]. However, there is rare research considering the atom-atom interaction between magnetic nanocrystals and the ligand itself and its structure-function relationship, particularly for biomedical imaging. Varela and co-workers have systemically investigated the underlying mechanism by which ligands tune the magnetism of nanoparticles involves atomic modulation at the surface of metal-oxide nanoparticles [38]. Typically, iron oxide NPs have a magnetically inactive surface layer due to structural and electronic differences compared to the bulk material. However, the application of organic acid ligands during high-temperature synthesis induces a significant change. The oxygen atoms from the organic acid cap the nanoparticle surface, forming O–Fe bonds. This atomic interaction effectively recreates the bulk-like environment on the surface, with the Fe ions bonded to the organic acid having a coordination and

distance from oxygen atoms that closely match those in the bulk [72, 73]. As a result, the density of states and occupancy of the iron's d orbitals at the surface become similar to those in the bulk, leading to a restoration of the surface magnetization. This atomic modulation by ligands not only preserves the high magnetization of the nanoparticles at room temperature but also enhances their potential for various applications, such as magnetic drug delivery and hyperthermia treatments. These findings underscore the importance of ligand design in tailoring the magnetic properties of nanoparticles through atomic-level surface engineering. Despite this interesting finding, the practical magnetism of nanocrystals is expected to be tuned toward enhancing biomedical applications.

To settle this dilemma, our group has recently developed a ligand-induced atomically segregation-tunable alloy nanoprobe (STAN)

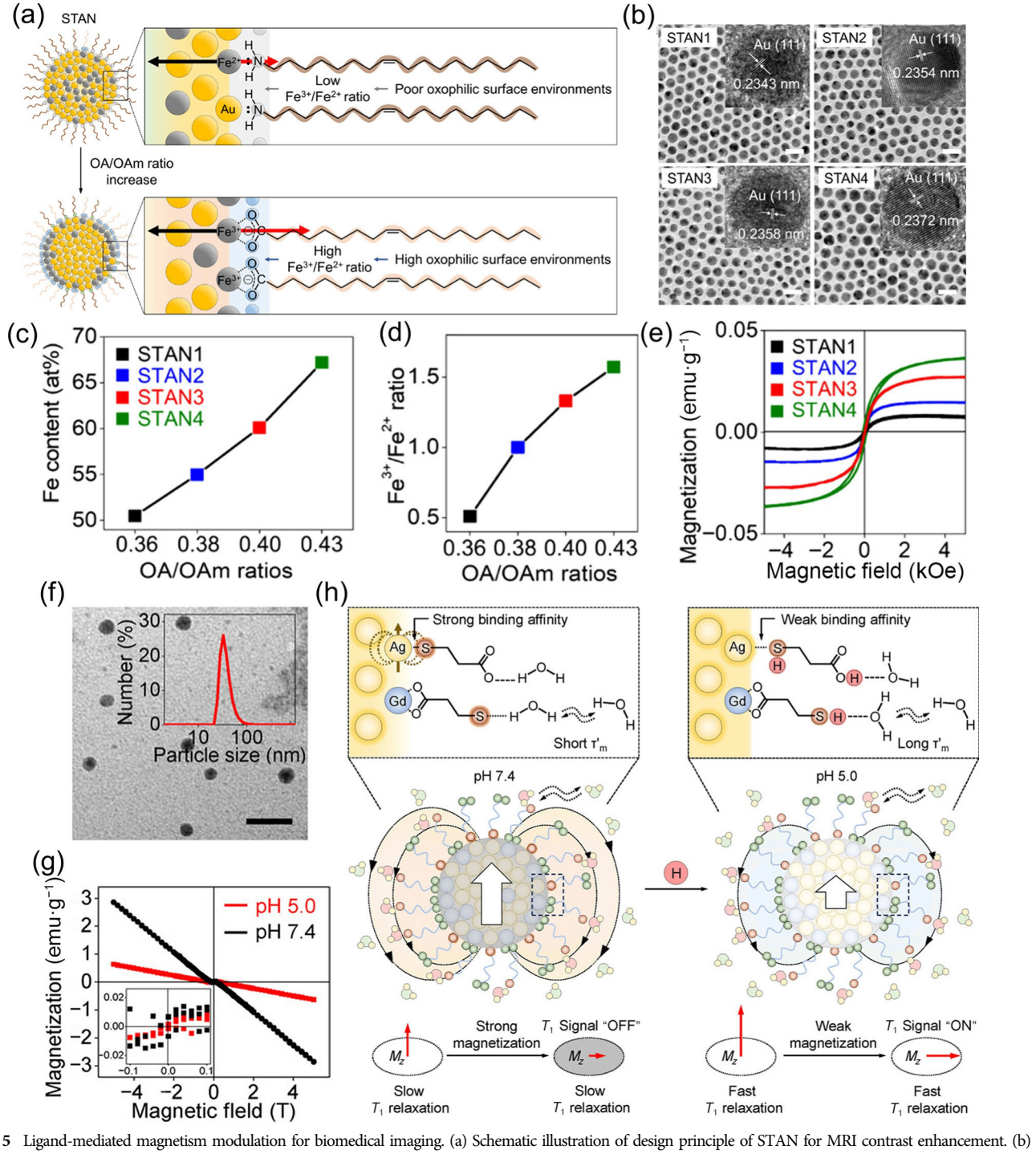

Figure 5 Ligand-mediated magnetism modulation for biomedical imaging. (a) Schematic illustration of design principle of STAN for MRI contrast enhancement. (b) TEM images of STANs, scale bar = 20 nm. Inset: HRTEM images of STANs, scale bar = 5 nm. (c) Surface Fe contents of STANs calculated by X-ray photoelectron spectroscopy (XPS). (d) Surface Fe^{3+}/Fe^{2+} ratios of STANs calculated by XPS. (e) M–H curves at 300 K for STANs. Reproduced with permission from Ref. [36], © American Chemical Society 2024. (f) TEM image of MCNPs, demonstrating their well-defined morphology (scale bar = 20 nm). Inset: size distribution analysis using dynamic light scattering (DLS), confirming the uniform size distribution of MCNPs. (g) M–H curves illustrating the magnetic behavior of MCNPs. (h) The underlying mechanism of pH-activatable MCNPs for UHF MRI. Reproduced with permission from Ref. [37], © Wiley-VCH GmbH 2024.

composed of bimetallic iron-gold nanoparticles for enhanced T_1 MR contrast (Fig. 5(a)) [36]. A series of ligand-induced atomically segregated alloy nanoprobes (namely STAN1, STAN2, STAN3, and STAN4) were synthesized by co-deposition of gold acetate and iron acetylacetonate in the presence of varying molar ratios of oleic acid (OA) to oleylamine (OAm) (Fig. 5(b)). Ligands with oxygenated groups were used to control the surface energy of iron in iron-gold nanoparticles. By adjusting the molar ratio of OA to OAm during synthesis, we were able to manipulate the oxidation state of iron on the particle surface. Detailly, a high ratio of OA to OAm created an oxophilic surface environment, which led to the oxidation of Fe from Fe^{2+} to Fe^{3+}. This process resulted in a strong driving force for Fe atoms to remain on the surface due to the relatively low surface energy of Fe^{3+} (Fig. 5(c)). Consequently, an increase in surface Fe content and the Fe^{3+}/Fe^{2+} ratio enhanced the surface magnetization and improved T_1 relaxivity, making the nanoparticles more effective for MRI contrast enhancement without the constraints of small particle size requirements (Figs. 5(d) and 5(e)). Besides the interactions between the ligand atoms and the nanoparticle, the reactive chemical properties of ligands also endow it with reactivity with specific substrates in lesions, which could realize a responsive magnetism switch for enhancing the sensitivity of MRI. For example, our group has recently reported a ligand-coated silver-gadolinium bimetallic nanoparticle, which can exhibit a switch from ferromagnetic to diamagnetic behavior in response to pH changes (Figs. 5(f) and 5(g)) [37]. At a neutral pH, the strong binding affinity between the silver atoms on the surface of the nanoparticle and the thiolate ($-S^-$) ligands results in a ferromagnetic state with substantial magnetization (Fig. 5(h)). This interaction also leads to weak hydrogen bonds between the ligands and water molecules, shortening the residency time (τ'_m) of water molecules in the second sphere and contributing to the nanoparticles' magnetic properties. In contrast, under acidic conditions typical of the tumor microenvironment, the thiolate ligands are protonated, transforming into thiol (–SH) ligands. This transformation significantly weakens the Ag–S binding affinity, reducing the nanoparticle's magnetization. Simultaneously, the protonation induces strong hydrogen bonds between the thiol groups and water molecules, thereby lengthening the τ'_m. This pH-responsive modulation of the ligand's binding affinity and hydrogen bonding interactions allows for the precise tuning of the nanoparticle's magnetic properties, enabling activatable MRI contrast enhancement at ultra-high field strengths.

3 Magnetism-modulated nanocrystals for biomedical imaging

The atomic-level structural design of nanocrystals embodies a sophisticated and targeted approach to modulating magnetic properties. This method stands apart from traditional macroscopic adjustment techniques, not only affording enhanced precision in structural tuning but also elucidating the intricate mechanisms that govern the relationship between structure and function. Such advancements hold immense promise for the development of high-performance nanoscale agents within the biomedical field, particularly in the realm of diagnostic imaging. Recent research work has compellingly showcased remarkable progress in the crafting of nanoprobes for medical diagnostics, with a keen emphasis on malignant tumor imaging, angiography, and neurological disease imaging [37, 48, 60, 74–76].

3.1 Tumor imaging

The application of atomically precise structural design of nanoprobes in tumor imaging covers the vast majority of biomedical use [77, 78]. Recently, our group has reported an antiferromagnetic nanoprobe (AFNP) capable of detecting microscopic primary hepatic tumors and micrometastases with high sensitivity (Fig. 6(a)) [53]. *Ex vivo* assessments, including GFP fluorescence imaging, hematoxylin and eosin (H&E) staining, and additional fluorescence microscopy, have confirmed the detection of microscopic primary liver tumors, measuring approximately 0.60 mm in diameter, through UHF-MRI (Figs. 6(b)–6(e)). These tumors were demarcated from surrounding healthy liver tissue with significantly increased ΔSNR (approximately 130.6%) observed at the 5 h post-injection of AFNP-RGD (Fig. 6(f)). Our investigation delved further to evaluate the nanoprobe's capabilities in a mouse model characterized by liver metastases. Even micrometastases, as diminutive as 0.20 mm and validated through both H&E staining and fluorescence imaging, were discernible via AFNP-RGD-enhanced UHF-MRI (Figs. 6(g)–6(j)). This achievement signifies an expansion of the detection capabilities for metastatic lesions. Notably, the UHF-MRI enhanced by AFNP-RGD was capable of identifying approximately 90.2% of metastases measuring less than 5 mm in diameter (Figs. 6(k) and 6(l)).

In a subsequent study, our group introduced a magnetic neutrality nanoprobe (MNN) enhanced by a doping-induced structural defect strategy, facilitating high-resolution UHF-MRI for the detection of previously undetectable minute lesions, such as isolated tumor cells (ITCs), in living mice (Fig. 7(a)) [48]. These MNNs exhibited an exceptionally low relaxivity ratio (r_2/r_1) of approximately 1.06 under 9 T MRI, setting a new benchmark for T_1 contrast agents in UHF-MRI. Utilizing a triple-negative breast cancer (TNBC) model, we administered intravenous injections of MNNs conjugated with a cyclic arginyl-glycyl-aspartic acid (RGD) peptide for targeted imaging. The MNN-RGD nanoprobes demonstrated significantly enhanced T_1 contrast *in vivo*, surpassing conventional T_1 contrast agents (Figs. 7(b) and 7(c)). The peak signal enhancement was observed at the tumor site 1.5 h post-injection (Fig. 7(d)). For the imaging of lung metastasis model, the MNN-RGD nanoprobes enable the noninvasive visualization of ITCs with a detection threshold of approximately 0.16 mm (Figs. 7(e)–7(h)). The capacity to detect ITCs at this early stage using MNNs has the potential to transform early diagnosis and treatment of metastatic diseases, thereby improving patient outcomes through more precise and timely therapeutic interventions.

In addition, with the emergence and the rapid progress of molecular imaging technology, the MRET nanoprobe has been considered a powerful tool for monitoring abnormally varied biomarkers, such as metal ions, enzymes, and nucleic acid, and thus diagnosing related diseases. These offered us more detailed information about the physiological and pathological process invasively, particularly the occurrence and progress of disease, which is highly crucial for treatment decisions and prognosis.

For example, Zhang and coworkers have introduced Fe_3O_4@Gd-DOTA NPs (called FFG NPs) for the noninvasive detection and differential diagnosis of malignant breast cancers, which presents a groundbreaking advancement in medical imaging [79]. These nanoprobes, integrating structural and molecular MRI functionalities, are designed to provide detailed visualization of both tumor structure and molecular changes associated with malignancy.

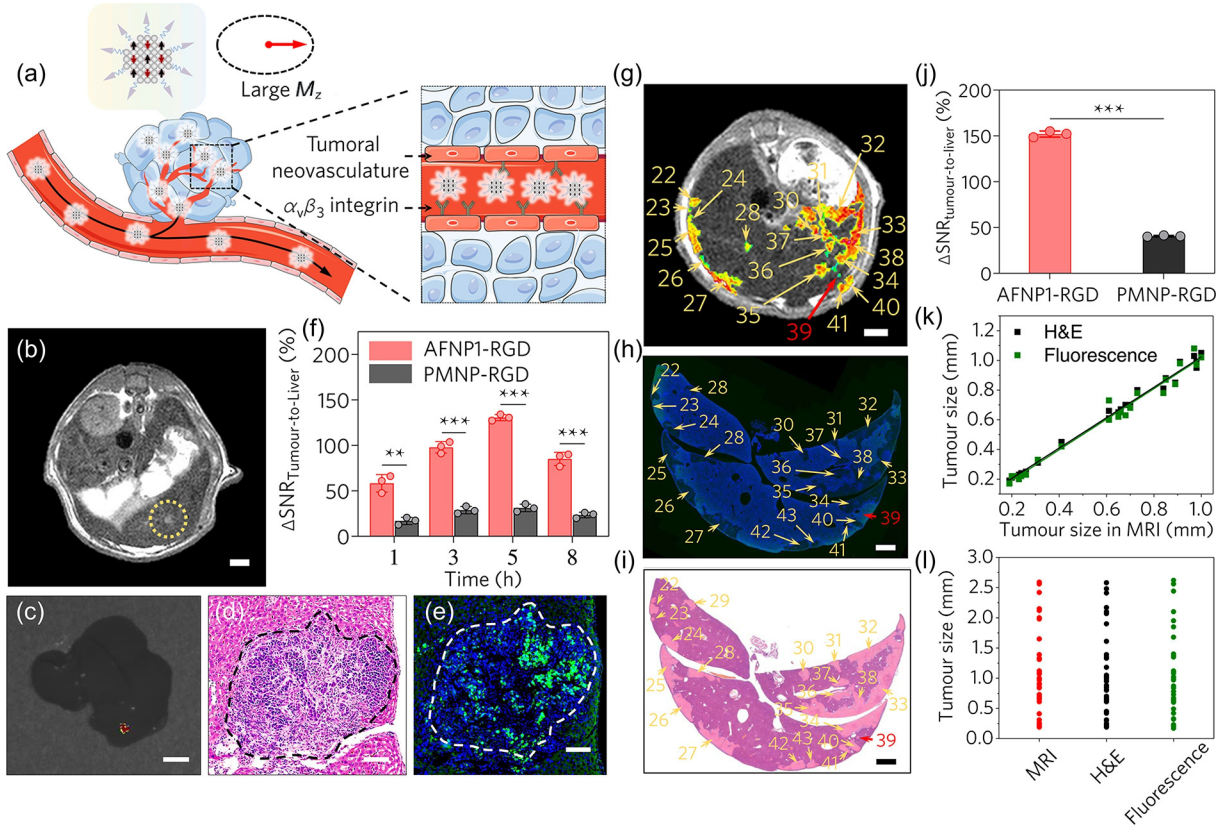

Figure 6 Metal alloying nanoprobes for tumor MRI. (a) Schematic diagram of targeted UHF MRI of microscopic primary tumors using AFNP-RGD. (b) T_1-*W* MR image of the mice-bearing microscopic primary hepatic tumor at 5 h post-injection (scale bar = 2 mm). (c) *Ex vivo* GFP fluorescence image of the dissected liver tissue at 5 h post-injection (scale bar = 5 mm). (d) H&E staining, and (e) fluorescence image of the microscopic primary tumor after the injection of AFNP-RGD (scale bar = 100 μm). (f) Quantitative analysis of ΔSNRs at various time points after intravenous injection. (g) T_1-*W* MR images, (h) fluorescence images (nuclei in blue and GFP in green) and (i) H&E-stained images of hepatic metastases-bearing mice at 5 h after the administration of AFNP1-RGD (scale bar = 2 mm for MRI; scale bar = 1000 μm for H&E-stained images and fluorescence images). (j) Quantification of ΔSNRs of MRI at 5 h after administration of AFNP1-RGD and PMNP-RGD. (k) The sizes of micrometastases (< 1 mm) detected by AFNP1-RGD enhanced MRI correlate well with those from H&E staining ($y = 1.0228x + 0.0004$; $R^2 = 0.989$) and fluorescence imaging ($y = 1.0284x - 0.0131$; $R^2 = 0.977$). (l) Sensitivity of AFNP1-RGD-enhanced MRI in detecting metastases (< 5 mm), based on the sizes of 4T1 metastatic tumors analyzed. Reproduced with permission from Ref. [53], © Liang, Z. et al. 2021.

The unique response of FFG NPs to furin, an enzyme overexpressed in cancer tissues, allows for enhanced T_1-*W* imaging, differentiating tumors based on furin levels. *In vitro* and *in vivo* studies have demonstrated the nanoprobes' high sensitivity, minimal toxicity, and rapid tumor accumulation, offering real-time, multidimensional imaging (Figs. 8(a)–8(d)). The dual-modality imaging capability of these nanoprobes is set to revolutionize personalized medicine in breast cancer treatment, enhancing diagnostic accuracy and potentially improving patient outcomes. Further, Song and co-workers have recently designed an activated afterglow/MRI probe as a companion diagnostics tool for dynamically assessing biomarker apurinic/apyrimidinic endonuclease 1 (APE1) during radiotherapy *in vivo* [80]. The authors developed a novel imaging strategy known as longitudinally and transversely subtraction-enhanced imaging (L&T-SEI), which significantly amplifies the contrast in MRI and enhances the signal-to-noise ratio between tumor and normal tissues in living mice (Figs. 8(e)–8(h)). This advanced technique, combined with afterglow imaging, provides a dual-modality approach that enables both anatomical and functional visualization of APE1 activity. The probe correlates afterglow and MRI signals with the expression levels of APE1, radiation dosage, intratumor reactive oxygen species (ROS), and DNA damage. This capability allows for the early prediction of radiotherapy outcomes, which can be detected as soon as 3 h post-treatment, a significant advancement over the traditional 6-day wait for observable tumor size reduction. Additionally, by monitoring APE1 levels, the probe facilitates the early and sensitive detection of liver organ injury, demonstrating superior performance compared to histopathological analysis (Fig. 8(i)). Moreover, the MRI component of this probe assesses APE1 expression in radiation-induced abscopal effects, offering valuable insights into the underlying biological mechanisms. This comprehensive imaging capability aids in the optimization of treatment protocols, marking a significant advancement in companion diagnostics for radiotherapy.

For externally ligand-mediated magnetism modulation, our group has presented a ligand-mediated magnetism-conversion nanoprobe (MCNP), which consisted of silver-gadolinium bimetallic nanoparticles coated with a 3-mercaptopropionic acid ligand [37]. Notably, the MCNP's pH-activatable relaxometric performance underscores the efficacy of this innovative approach. A pronounced enhancement in the r_1 relaxivity value of the MCNP was observed at an acidic pH, reaching 10.6 $mM^{-1}·s^{-1}$, which is a remarkable 10-fold increase compared to its value at neutral pH, as measured under a 9 T MR scanner (Figs. 9(a)–9(c)). Then, the RGD functionalized MNCP (MCNP-RGD) was intravenously

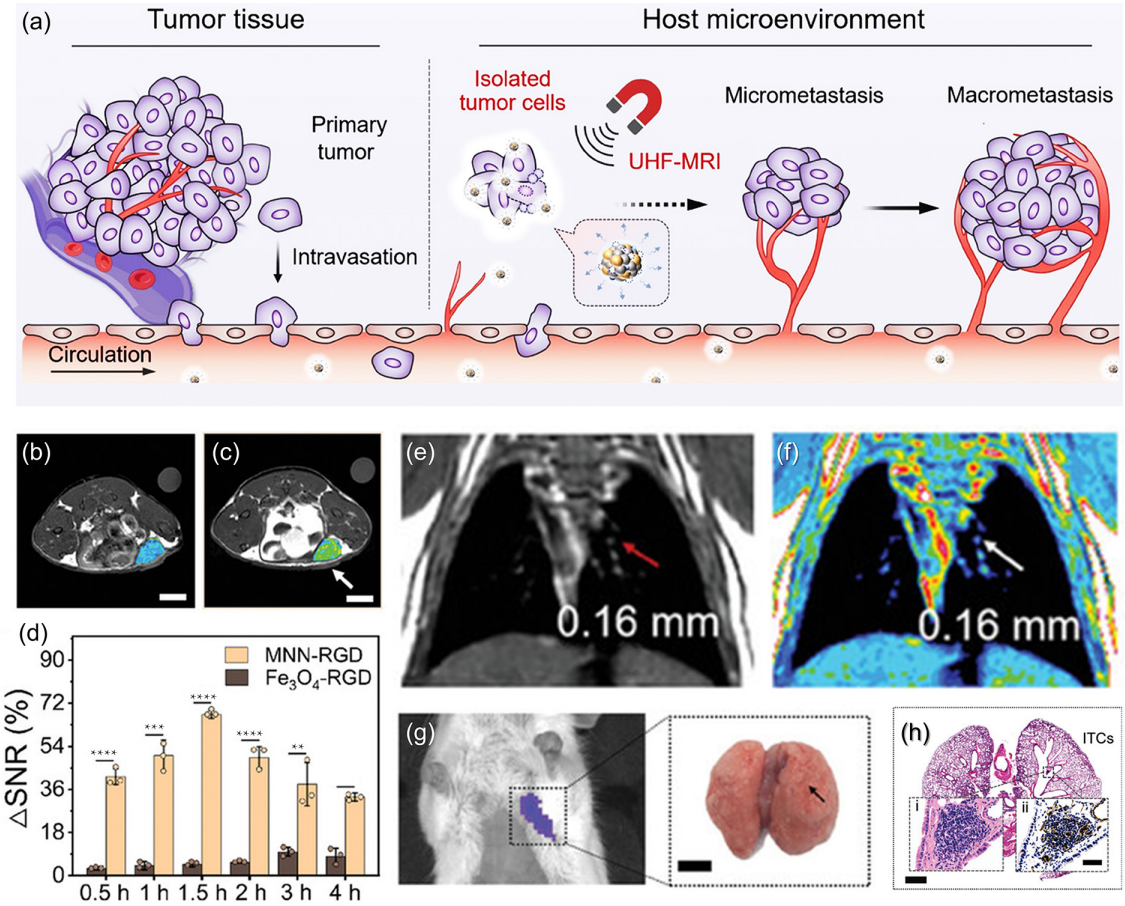

Figure 7 Metal ion doped nanocrystals for tumor MRI. (a) Schematic illustration of identification of ITCs based on MNN-enhanced UHF T_1 imaging. The color-coded T_1-*W* MR images of 4T1-Luc tumor-bearing BALB/c mice before and after intravenous administration of (b) Fe_3O_4-RGD and (c) MNN-RGD nanoprobes (5 mg·kg^{-1} [Fe]) at 1.5 h post-injection. Scale bar = 4 mm. (d) The quantification analysis of signal changes in tumors at different time points after treatment with MNN-RGD and Fe_3O_4-RGD nanoprobes. (e) T_1-*W* and and the color-coded MR images at 1 h post-injection with MNN-RGD nanoprobes (slice orientation: coronal, [Fe] = 5.0 mg·kg^{-1}, scale bar = 4 mm), and (g) bioluminescence imaging (BLI) images of lung metastases (scale bar = 4 mm), *ex vivo* images (scale bar = 2 mm), and (h) H&E staining images (scale bar = 1 mm) of the lung. Inset: (i) H&E-stained image and (ii) CD31-stained image of ITCs in lung (scale bar = 400 μm). Reproduced with permission from Ref. [48], © Wiley-VCH GmbH 2024.

injected into mice bearing primary hepatic tumor to evaluate the pH activatable MRI performance *in vivo*, which realized clear differentiation of the primary tumor from the surrounding normal liver tissue (Figs. 9(d)–9(f)). To our knowledge, this represents the pioneering demonstration of manipulating the binding affinities between the surface atoms and the ligand anchoring groups, thereby artificially modulating the intrinsic magnetism of nano contrast agents in response to specific stimuli.

3.2 Microvessel imaging

Generally, high-resolution microvessel imaging with angiography is essential for diagnosing and treating diseases affecting the brain, heart, and other areas [81–86]. For example, cerebral artery blockages, often a cause of ischemic strokes, and peripheral vessel obstructions, which can lead to limb loss or death, highlight the urgency [87–90]. Coronary artery imaging is identically vital due to its link with global mortality [91, 92]. However, achieving this level of detail remains a challenge with current MRI technology. Recently, Fan and coworkers have reported the synthesis and modification of $Zn_{0.4}Fe_{2.6}O_4$ nanoparticles with different surface potentials using ligands such as DA (dopamine), DHCA (dehydrocholic acid), and PO-mPEG (polyethylene glycol) (Fig. 10(a)) [76]. These modifications were explored to enhance the T_1 MRI characteristics of the nanoparticles in the context of rabbit carotid atherosclerotic plaques (Figs. 10(b) and 10(c)). The findings from both *in vivo* and *in vitro* experiments demonstrate that by altering the surface potential of $Zn_{0.4}Fe_{2.6}O_4$, the nanoparticles' affinity for macrophages within the plaque can be precisely adjusted. This tailoring significantly improves the diagnostic capabilities of MRI for atherosclerosis. Furthermore, the study introduced an optimized method for creating rabbit carotid atherosclerotic plaque models, which allows for the precise colocalization of plaque positions on both MRI images and pathology slides, thereby facilitating more accurate diagnosis and treatment planning.

3.3 Neurological diseases imaging

Neurological disorders, such as epilepsy, Alzheimer's disease (AD), and Parkinson's disease (PD), impose severe limitations and are fatal to millions annually [93, 94]. These conditions often lead to driving and employment restrictions, social isolation, and psychological distress for those affected. Diagnostic brain imaging is crucial for identifying neurological diseases at an early stage, facilitating timely treatment. In clinical settings, computed

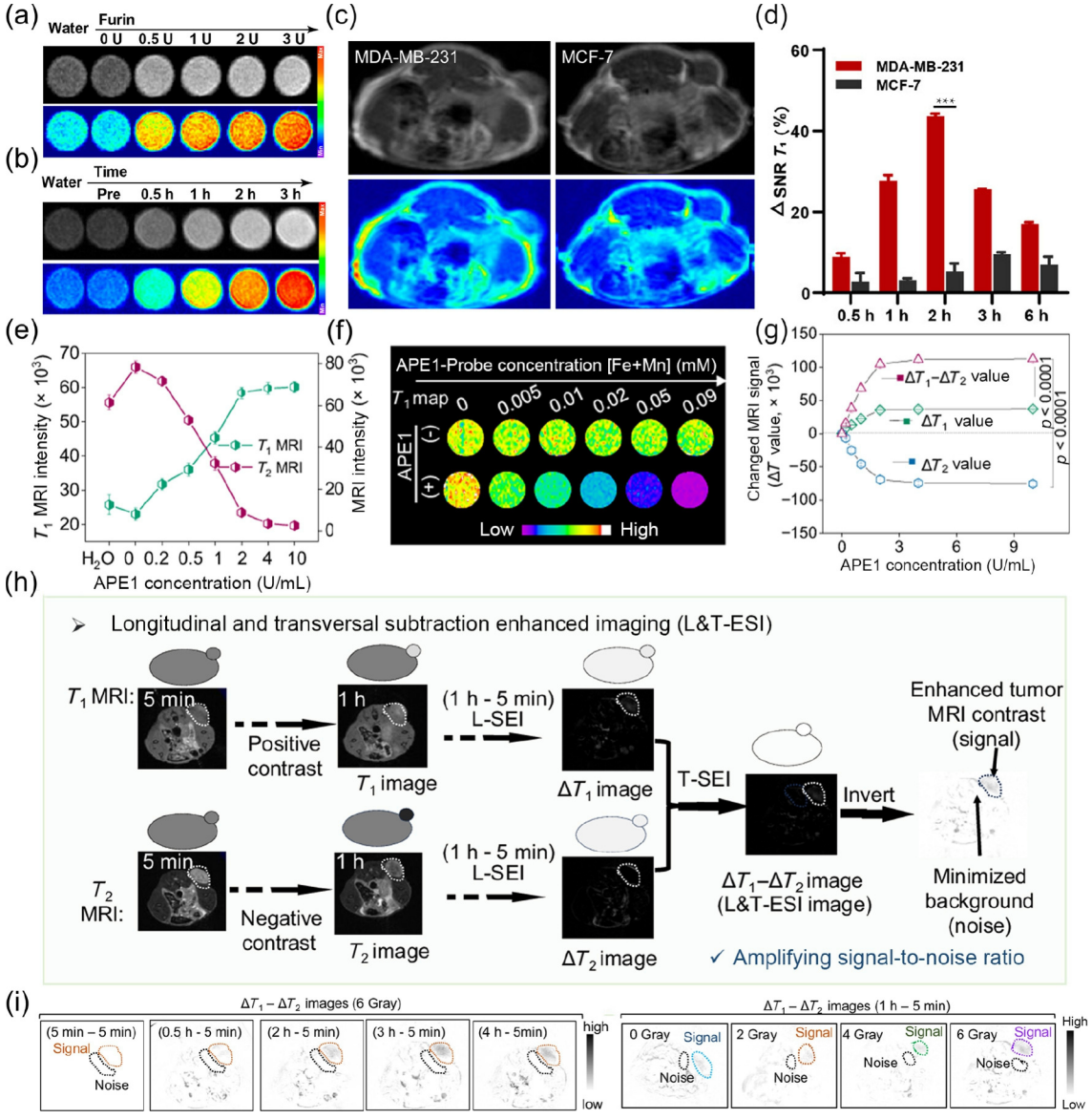

Figure 8 MRET nanoprobes for tumor MRI. T_1-*W* and the color-coded MRI images of FFG NPs supernatant (magnetic separation) (a) with the increase in the enzyme activity of furin and (b) with the increase in the furin catalysis time. (c) T_1-*W* (top) and the color-coded (bottom) MR images for the MDA-MB-231 (left) and MCF-7 (right) tumors. (d) Quantitative measurement of T_1 MR images for the MDA-MB-231 and MCF-7 tumors. Reproduced with permission from Ref. [79], © American Chemical Society 2024. (e) T_1 and T_2 MRI signal intensity of APE1-probe treated with various concentrations of APE1. (f) Relaxation time mapping images of different concentrations of APE1-probe before and after APE1 (10 U·mL^{-1}) incubation. (g) MRI signal range (ΔT_1, ΔT_2, and $\Delta T_1 - \Delta T_2$ value) of APE1-probe treated with various concentrations of APE1. (h) Scheme illustration and L&T-SEI images of mice with 6 Gray radiation treatment and APE1-probe injection. (i) L&T-ESI images of tumor with various radiation dose treatment (left) and with 6 Gray of radiation dose treatment at different time points (right). Reproduced with permission from Ref. [80], © Yue, R. et al. 2024.

tomography (CT), positron emission computed tomography (PET), and MRI are primary imaging techniques for neurological conditions [95, 96]. While CT and PET potentially leading to radiation damage, MRI utilizes strong magnetic fields and radiofrequency pulses to generate high-resolution soft tissue images [97, 98]. This makes MRI a safer and more effective option for diagnosing disorders affecting the brain, spinal cord, and joints [99]. However, MRI's inherent limited sensitivity and prolonged scan times can hinder the early detection of neurological diseases. To overcome these challenges, the burgeoning field of nanotechnology has led to the development of various magnetic nanoprobes as contrast agents, which significantly enhance image contrast by reducing the relaxation times of water protons, thereby improving diagnostic accuracy [100–102]. For example, Li et al. have developed a T_1-*W* contrast agent, termed the electrically responsive hybrid micelle (EM), predicated on the magnetic resonance tuning (MRET) effect, leveraging a superparamagnetic iron oxide cluster encased in a paramagnetic polymer coating (Figs. 11(a) and 11(b)) [74]. This agent transcends the blood-brain barrier, affording heightened sensitivity and a pronounced target-to-background ratio. It is responsive to the electric-field changes in the brain associated with seizures, which triggers the breakdown of the agent and restores the T_1-*W* MRI signal. This allows for the detection of seizure foci that may be undetectable with conventional MRI. The MR phantom study demonstrated that the T_1-*W* MR signals from both the blank micelles (BMs) without encapsulated ultrasmall

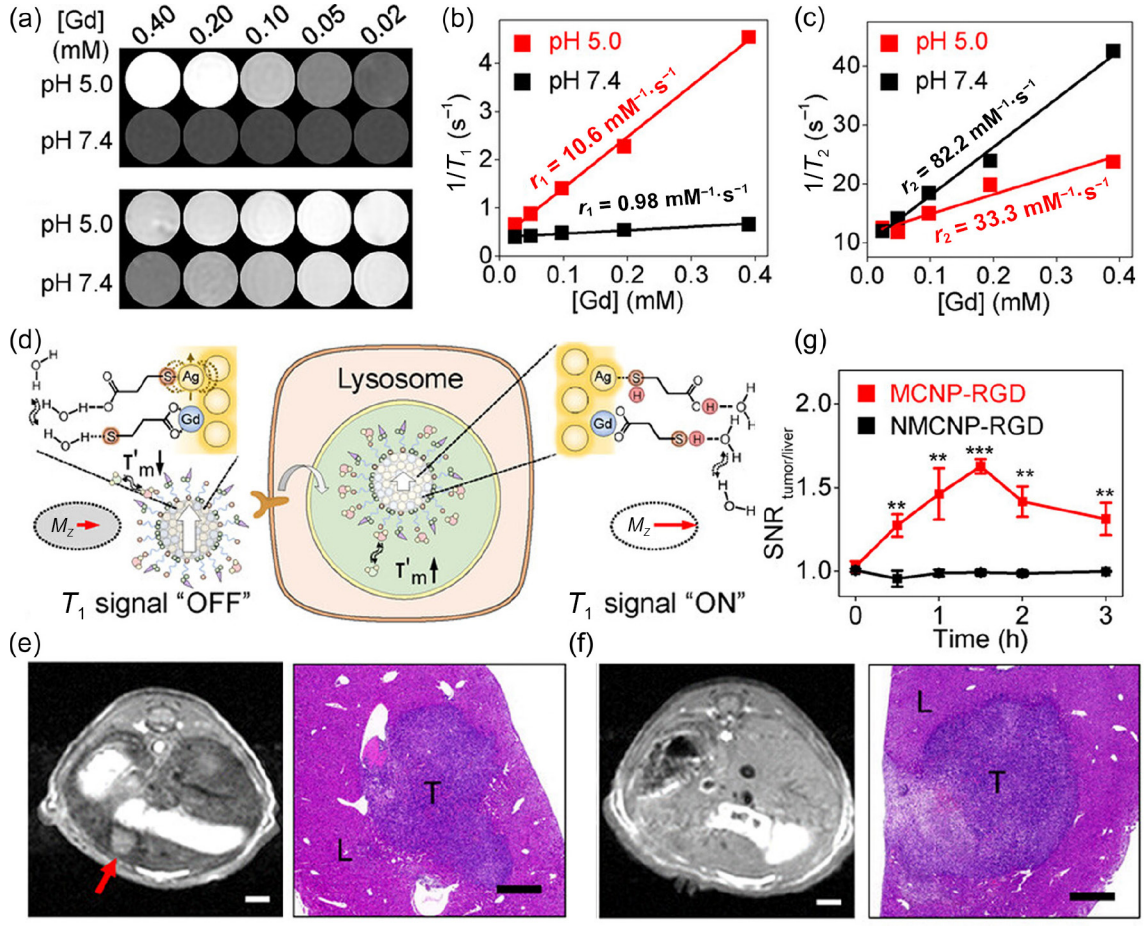

Figure 9 Ligand-mediated magnetism-conversion nanoprobes for tumor MRI. (a) T_1-*W* (top), and T_2-*W* (bottom) MR images of MCNPs at pH 7.4 and 5.0. The corresponding (b) T_1 relaxation rate ($1/T_1$, s^{-1}) and (c) T_2 relaxation rate ($1/T_2$, s^{-1}) plotted against Gd concentration (mM) for MCNPs at pH 7.4 and 5.0. (d) Schematic illustration depicting the MR imaging using MCNP-RGD. Transverse T_1-*W* MR images and H&E staining image of primary hepatic tumor-bearing nude mice after intravenous injection of (e) MCNP-RGD or (f) NMCNP-RGD (0.2 mmol·kg^{-1} [Gd]) at a 9 T MRI scanner (scale bar = 2 mm). (g) Quantitative analysis of SNR at the corresponding time points after administration of MCNP-RGD or NMCNP-RGD. Reproduced with permission from Ref. [37], © Wiley-VCH GmbH 2024.

superparamagnetic iron oxide (USPIO) and Gd-DTPA increased in direct proportion to the Gd^{3+} concentration, ranging from 0.008 to 0.2 mM. In contrast, the MR signal enhancement for EM was negligible (Fig. 11(c)). When an external electric field (with 100–500 μA) was applied, the structure of EM was disintegrated and the T_1 signal was dramatically recovered, while no MR signal variations were detected for the CMs or Gd^{3+}-DTPA (Fig. 11(d)). The study demonstrates the effectiveness of this agent in mouse models of acute and chronic seizure (Figs. 11(e) and 11(f)), suggesting its potential to improve the diagnosis and surgical planning for epilepsy in patients with non-distinctive MRI lesions. The contrast agent's ability to convert excessive neuronal discharge into a visual T_1-*W* MRI signal could significantly increase the probability of detecting seizure foci and facilitate the study of brain diseases associated with epilepsy.

4 Conclusions and perspectives

Overall, atomic-level magnetism modulation of inorganic nanocrystals offers unprecedented precision for optimizing their performance in biomedical imaging. The strategies of metal alloying, ion doping, distance-dependent magnetic interactions, and ligand-mediated superficial magnetism modulation with atomical precision have proven to be potent in crafting nanoparticles with tailored magnetic responses. The meticulous engineering of these nanocrystals, as discussed in the preceding sections, has unveiled a plethora of opportunities for advancing diagnostic capabilities, particularly in the early detection and precise visualization of malignant tumors, and other biomedical applications. Nevertheless, while significant progress has been made in the development of nanocrystals with atomically controlled magnetic properties, several challenges remain, including, but not limited to the restricted enhancement in performance, inefficient screening methods, scalable production methods, and the potential toxicity associated with their use. Addressing these challenges is crucial for the successful translation of this technology into clinical practice.

(1) Although atomic-level magnetic modulation offers greater precision compared to traditional mesoscopic-level regulation, the extent of its enhancement in the imaging performance of nanocrystals is limited. Generally, a single nanoparticle possesses hundreds or thousands of atoms in the bulk phase, where merely bits of external atoms could be doped into the proper site for stabilizing the total energy, thus giving rise to inapparent interactions with the whole system. Similarly, the ligand-mediated transfer of electrons mainly occurred in the surface layer of nanocrystals, while the structure of the bulk phase was subject to minimal impact, which means constrained magnetism variation. Accordingly, these necessitate the development of nanoprobes that

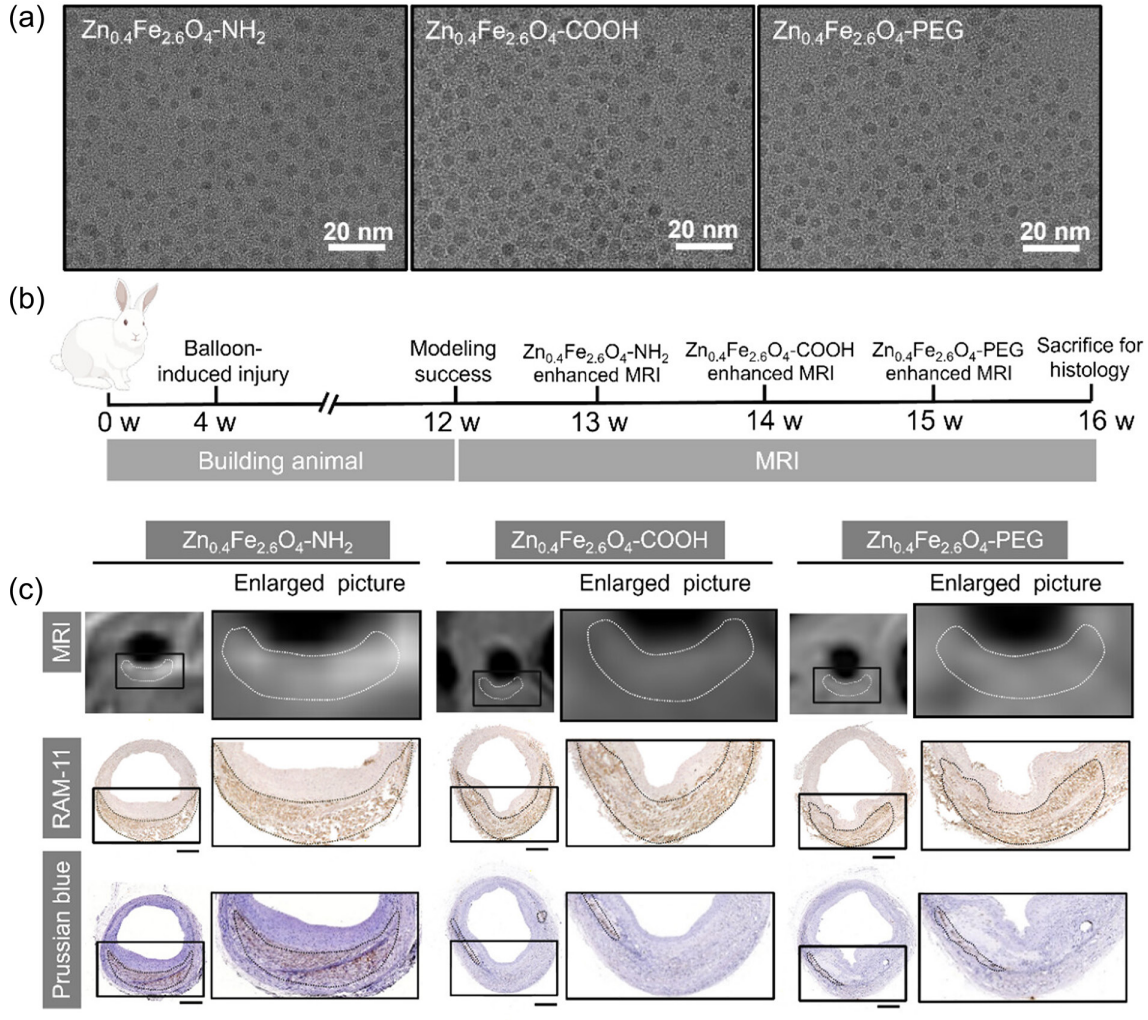

Figure 10 Metal ion doped nano contrast agents for microvessel MRI. (a) TEM images $Zn_{0.4}Fe_{2.6}O_4$ with different surface coating. (b) Schematic diagram of administration process for MRI of rabbit carotid atherosclerosis models. (c) T_1-*W* images of right carotid artery after injection of $Zn_{0.4}Fe_{2.6}O_4$–NH_2, $Zn_{0.4}Fe_{2.6}O_4$–COOH, and $Zn_{0.4}Fe_{2.6}O_4$–PEG at 10 min; corresponding photographs of plaques were stained by RAM11 and Prussian blue. Scale bars = 500 μm. Reproduced with permission from Ref. [76], © American Chemical Society 2024.

are smaller in size than their current counterparts. Metal nanoclusters assembled with nearly dozens or hundreds of metal atoms fill the gap between discrete atoms and bigger nanoparticles, providing unique opportunities for investigating the quantum effects and precise structure-property correlations at the atomic level [103]. Considering their extremely small size, subtle changes in structure or surface ligands can cause significant variations of physiochemical properties, thus offering the potential to construct high-performance probes.

(2) The existing literature has illustrated the effective utilization of specific external atoms in enhancing the magnetic properties of exemplary nanocrystals. However, a clear methodology for determining the optimal combination of these external atoms and nanocrystal configurations to achieve superior material performance is yet to be established. While traditional material screening has relied heavily on trial-and-error approaches, recent advancements in artificial intelligence (AI), particularly machine learning, are revolutionizing the field [104, 105]. Machine learning employs data-driven strategies to uncover patterns within extensive datasets, integrating theoretical knowledge with empirical data to bridge the divide between theoretical models and practical applications [106, 107]. This approach could elucidate the structure-function relationships by constructing surrogate models based on existing features and further predict the properties of arbitrary nanoprobe configurations, thereby expediting the identification of high-performance nanoprobes [106, 108, 109]. These innovations are expected to greatly accelerate the discovery of innovative nanoprobes and to efficiently identify material and parameter combinations that enhance imaging contrast for advanced biomedical imaging, thereby marking a new era in the precision and efficiency of nanoprobe development.

(3) Reproducibility and the ability to scale up the production of nanocrystals continue to pose significant challenges within the realm of materials science [110–113]. While atomically precise nanoprobes, characterized by their nanoscale dimensions, can be successfully synthesized at the laboratory scale, several factors hinder their large-scale production. These include the complexity of the manufacturing processes, the time-intensive nature of screening procedures, the necessity for specialized equipment, and the variability between different batches. Furthermore, ensuring the colloidal stability and maintaining the physicochemical robustness of these nanoprobes are critical for their transportation and long-

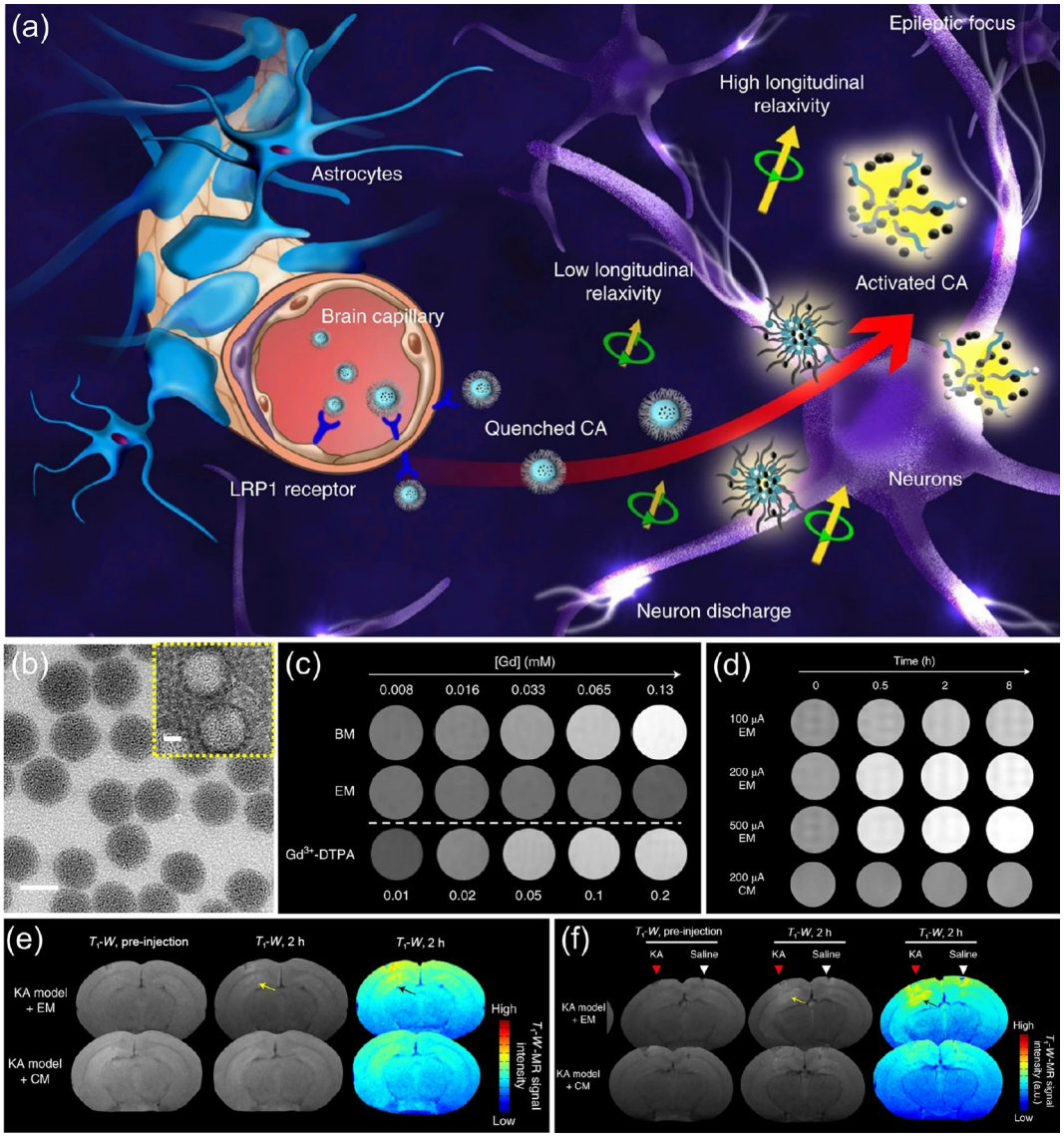

Figure 11 MRET nanoprobes for epilepsy MRI. (a) Schematic illustration of non-invasive visualization of the epileptic focus with an electrically responsive T_1-*W* MR contrast agent. (b) TEM image of EMs. (c) T_1-*W* MR phantom images of EMs, BMs and Gd^{3+}-DTPA as a function of Gd^{3+} concentration. (d) T_1-*W* MR phantom images of EMs and CMs as functions of current intensity and application time. Representative T_1-*W* and color-coded MR images of the (e) chronic seizure model brains and (f) acute seizure model brains at selected time points post-injection of EMs or CMs. Reproduced with permission from Ref. [74], © Wang, C. et al. under exclusive licence to Springer Nature Limited 2020.

term storage, which are essential for their practical application and commercial viability.

(4) The incorporation of dopant atoms into recognized nanocrystals has the potential to enhance their performance in bioimaging applications. However, the potential leakage of these inorganic metallic atoms poses an unpredictable risk to living organisms, which may have serious implications for their biocompatibility [49]. Conversely, the newly reported ligand-mediated magnetism modulation presents a promising alternative. This method not only holds the potential to optimize performance but also addresses concerns related to biosafety, thereby offering a more viable strategy for the development of nanocrystals intended for biological applications [114]. Therefore, further exploration into this area is warranted to fully harness its potential.

All in all, the advancement of methods for the precise atomic control of nanocrystals' magnetism can yield profound insights into the correlation between the structural attributes and functional performance of magnetic nanomaterials. This development may facilitate a paradigm shift in the diagnostic applications for various diseases.

Data availability

All data needed to support the conclusions in the paper are presented in the manuscript. Additional data related to this paper may be requested from the corresponding author upon request.

Acknowledgements

This work was supported by the National Natural Science Foundation of China (No. 62027901), the National Key Research and Development Program of China (Nos. 2022YFB3203801, 2022YFB3203804, and 2022YFB3203800), the National Natural

Science Foundation of China (Nos. 32071374, and 22305151), Program of Shanghai Academic Research Leader under the Science and Technology Innovation Action Plan (No. 21XD1422100), the Leading Talent of "Ten Thousand Plan"-National High-Level Talents Special Support Plan, Program of Shanghai Science and Technology Development (No. 22TS1400700), the Natural Science Foundation of Zhejiang Province (No. LR22C100001), the Innovative Research Team of High-level Local Universities in Shanghai (No. SHSMUZDCX20210900) and the CAS Interdisciplinary Innovation Team (No. JCTD-2020-08).

Declaration of competing interest

All the contributing authors report no conflict of interests in this work.

Author contribution statement

Y. H. G.: Writing manuscript, revising manuscript. H. D.: Revising manuscript. Q. Y. W.: Revising manuscript. F. Y. L.: Project administration, funding acquisition. D. S. L.: Project administration, funding acquisition. All the authors have approved the final manuscript.

Informed consent

Not applicable.

Ethics statement

Not applicable.

Use of AI statement

During the preparation of this work, the authors used Kimi Chat in order to polish the language to enhance the readability of the text while retaining the original meaning. After using this tool/service, the authors reviewed and edited the content as needed and take full responsibility for the content of the publication.

References

[1] Wu, G.; Zelenay, P. Activity versus stability of atomically dispersed transition-metal electrocatalysts. *Nat. Rev. Mater.* **2024**, *9*, 643–656.

[2] Santos, P. J.; Gabrys, P. A.; Zornberg, L. Z.; Lee, M. S.; Macfarlane, R. J. Macroscopic materials assembled from nanoparticle superlattices. *Nature* **2021**, *591*, 586–591.

[3] Jain, R.; Lakhnot, A. S.; Bhimani, K.; Sharma, S.; Mahajani, V.; Panchal, R. A.; Kamble, M.; Han, F. D.; Wang, C. S.; Koratkar, N. Nanostructuring versus microstructuring in battery electrodes. *Nat. Rev. Mater.* **2022**, *7*, 736–746.

[4] Ma, B. J.; Bianco, A. Regulation of biological processes by intrinsically chiral engineered materials. *Nat. Rev. Mater.* **2023**, *8*, 403–413.

[5] Zheng, Y.; Slade, T. J.; Hu, L.; Tan, X. Y.; Luo, Y. B.; Luo, Z. Z.; Xu, J. W.; Yan, Q. Y.; Kanatzidis, M. G. Defect engineering in thermoelectric materials: What have we learned. *Chem. Soc. Rev.* **2021**, *50*, 9022–9054.

[6] Lu, C.; Han, L. B.; Wang, J.; Wan, J. C.; Song, G. S.; Rao, J. H. Engineering of magnetic nanoparticles as magnetic particle imaging tracers. *Chem. Soc. Rev.* **2021**, *50*, 8102–8146.

[7] Hang, Y. J.; Wang, A. Y.; Wu, N. Q. Plasmonic silver and gold nanoparticles: Shape- and structure-modulated plasmonic functionality for point-of-caring sensing, bio-imaging and medical therapy. *Chem. Soc. Rev.* **2024**, *53*, 2932–2971.

[8] Chen, J. J.; Xie, H.; Liu, L. Z.; Guan, H.; You, Z. S.; Zou, L. J.; Jin, H. J. Strengthening gold with dispersed nanovoids. *Science* **2024**, *385*, 629–633.

[9] Liu, X. Y.; Lyu, D.; Merlet, C.; Leesmith, M. J. A.; Hua, X.; Xu, Z.; Grey, C. P.; Forse, A. C. Structural disorder determines capacitance in nanoporous carbons. *Science* **2024**, *384*, 321–325.

[10] Zhou, Y. Y.; Herz, L. M.; Jen, A. K. Y.; Saliba, M. Advances and challenges in understanding the microscopic structure-property-performance relationship in perovskite solar cells. *Nat. Energy* **2022**, *7*, 794–807.

[11] Hu, X.; Zhang, B.; Zhang, M.; Liang, W. S.; Hong, B. Z.; Ma, Z. Y.; Sheng, J. P.; Liu, T. Q.; Yang, S. F.; Liang, Z. Y. et al. An artificial metabzyme for tumour-cell-specific metabolic therapy. *Nat. Nanotechnol.* **2024**, *19*, 1712–1722.

[12] Guan, Q. Q.; Zhu, C. W.; Lin, Y.; Vovk, E. I.; Zhou, X. H.; Yang, Y.; Yu, H. C.; Cao, L. N.; Wang, H. W.; Zhang, X. H. et al. Bimetallic monolayer catalyst breaks the activity-selectivity trade-off on metal particle size for efficient chemoselective hydrogenations. *Nat. Catal.* **2021**, *4*, 840–849.

[13] Roca, A. G.; Gutiérrez, L.; Gavilán, H.; Fortes Brollo, M. E.; Veintemillas-Verdaguer, S.; Morales, M. D. P. Design strategies for shape-controlled magnetic iron oxide nanoparticles. *Adv. Drug Deliv. Rev.* **2019**, *138*, 68–104.

[14] Ni, D. L.; Bu, W. B.; Ehlerding, E. B.; Cai, W. B.; Shi, J. L. Engineering of inorganic nanoparticles as magnetic resonance imaging contrast agents. *Chem. Soc. Rev.* **2017**, *46*, 7438–7468.

[15] Jeon, M.; Halbert, M. V.; Stephen, Z. R.; Zhang, M. Q. Iron oxide nanoparticles as T_1 contrast agents for magnetic resonance imaging: Fundamentals, challenges, applications, and prospectives. *Adv. Mater.* **2021**, *33*, 1906539.

[16] Xie, X. L.; Zhai, J.; Zhou, X. Y.; Guo, Z. J.; Lo, P. C.; Zhu, G. Y.; Chan, K. W. Y.; Yang, M. S. Magnetic particle imaging: From tracer design to biomedical applications in vasculature abnormality. *Adv. Mater.* **2024**, *36*, 2306450.

[17] Zhao, Z. H.; Li, M. Y.; Zeng, J.; Huo, L. L.; Liu, K.; Wei, R. X.; Ni, K. Y.; Gao, J. H. Recent advances in engineering iron oxide nanoparticles for effective magnetic resonance imaging. *Bioact. Mater.* **2022**, *12*, 214–245.

[18] Zhou, Z. J.; Yang, L. J.; Gao, J. H.; Chen, X. Y. Structure-relaxivity relationships of magnetic nanoparticles for magnetic resonance imaging. *Adv. Mater.* **2019**, *31*, 1804567.

[19] Hadadian, Y.; Masoomi, H.; Dinari, A.; Ryu, C.; Hwang, S.; Kim, S.; Cho, B. K.; Lee, J. Y.; Yoon, J. From low to high saturation magnetization in magnetite nanoparticles: The crucial role of the molar ratios between the chemicals. *ACS Omega* **2022**, *7*, 15996–16012.

[20] Ma, Z. H.; Mohapatra, J.; Wei, K. C.; Liu, J. P.; Sun, S. H. Magnetic nanoparticles: Synthesis, anisotropy, and applications. *Chem. Rev.* **2023**, *123*, 3904–3943.

[21] Tay, Z. W.; Savliwala, S.; Hensley, D. W.; Fung, K. L. B.; Colson, C.; Fellows, B. D.; Zhou, X. Y.; Huynh, Q.; Lu, Y.; Zheng, B. et al. Superferromagnetic nanoparticles enable order-of-magnitude resolution & sensitivity gain in magnetic particle imaging. *Small Methods* **2021**, *5*, 2100796.

[22] Wang, Q. Y.; Ma, X. B.; Liao, H. W.; Liang, Z. Y.; Li, F. Y.; Tian, J.; Ling, D. S. Artificially engineered cubic iron oxide nanoparticle as a high-performance magnetic particle imaging tracer for stem cell tracking. *ACS Nano* **2020**, *14*, 2053–2062.

[23] Song, G. S.; Kenney, M.; Chen, Y. S.; Zheng, X. C.; Deng, Y.; Chen, Z.; Wang, S. X.; Gambhir, S. S.; Dai, H. J.; Rao, J. H. Carbon-coated FeCo nanoparticles as sensitive magnetic-particle-imaging tracers with photothermal and magnetothermal properties. *Nat. Biomed. Eng.* **2020**, *4*, 325–334.

[24] Zeng, J.; Huo, L. L.; Wang, Z. Y.; Sun, X.; Guo, Y.; Li, M. Y.; Tan, M. Y.; Zhu, S. Q.; Fang, J. Q.; Zhao, Z. H. Effect of hollow structures on T_1 and T_2 relaxivities and their application in accurate tumor imaging. *Chem. Mater.* **2023**, *35*, 7643–7654.

[25] Abdibastami, A.; Gloag, L.; Prada, J. P.; Duong, H. T. K.; Shanehsazzadeh, S.; Sulway, S. A.; Cheong, S.; Hackbarth, H.; Bedford, N. M.; Jameson, G. N. L. et al. How size and composition of cobalt doped iron oxide nanoparticle tracers enhance magnetic particle imaging performance. *Chem. Mater.* **2024**, *36*, 8773–8781.

[26] Nguyen, M. D.; Deng, L. Z.; Lee, J. M.; Resendez, K. M.; Fuller, M.; Hoijang, S.; Robles-Hernandez, F.; Chu, C. W.; Litvinov, D.; Hadjiev, V. G. et al. Magnetic tunability via control of crystallinity and size in polycrystalline iron oxide nanoparticles. *Small* **2024**, *20*, 2402940.

[27] Mao, Y.; Li, Y.; Zang, F. C.; Yu, H. L.; Yan, S.; Song, Q. S.; Qin, Z. G.; Sun, J. F.; Chen, B.; Huang, X. et al. Continuous synthesis of extremely small-sized iron oxide nanoparticles used for T_1-weighted magnetic resonance imaging via a fluidic reactor. *Sci. China Mater.* **2022**, *65*, 1646–1654.

[28] Piché, D.; Tavernaro, I.; Fleddermann, J.; Lozano, J. G.; Varambhia, A.; Maguire, M. L.; Koch, M.; Ukai, T.; Hernández Rodríguez, A. J.; Jones, L. et al. Targeted T_1 magnetic resonance imaging contrast enhancement with extraordinarily small $CoFe_2O_4$ nanoparticles. *ACS Appl. Mater. Interfaces* **2019**, *11*, 6724–6740.

[29] Novoa, J. J.; Deumal, M.; Jornet-Somoza, J. Calculation of microscopic exchange interactions and modelling of macroscopic magnetic properties in molecule-based magnets. *Chem. Soc. Rev.* **2011**, *40*, 3182–3212.

[30] Zhao, J. J.; Huang, X. M.; Jin, P.; Chen, Z. F. Magnetic properties of atomic clusters and endohedral metallofullerenes. *Coordin. Chem. Rev.* **2015**, *289–290*, 315–340

[31] Yang, Y.; Chen, C. C.; Scott, M. C.; Ophus, C.; Xu, R.; Pryor, A.; Wu, L.; Sun, F.; Theis, W.; Zhou, J. H. et al. Deciphering chemical order/disorder and material properties at the single-atom level. *Nature* **2017**, *542*, 75–79.

[32] González-Herrero, H.; Gómez-Rodríguez, J. M.; Mallet, P.; Moaied, M.; Palacios, J. J.; Salgado, C.; Ugeda, M. M.; Veuillen, J. Y.; Yndurain, F.; Brihuega, I. Atomic-scale control of graphene magnetism by using hydrogen atoms. *Science* **2016**, *352*, 437–441.

[33] Zheng, B. Z.; Fan, J. Y.; Chen, B.; Qin, X.; Wang, J.; Wang, F.; Deng, R. R.; Liu, X. G. Rare-earth doping in nanostructured inorganic materials. *Chem. Rev.* **2022**, *122*, 5519–5603.

[34] Cao, C. C.; Zhu, L.; Meng, Y.; Zhai, X. B.; Wang, Y. G. Atomic level structural modulation during the structural relaxation and its effect on magnetic properties of $Fe_{81}Si_4B_{10}P_4Cu_1$ nanocrystalline alloy. *J. Magn. Magn. Mater.* **2018**, *456*, 274–280.

[35] Gan, Y. H.; Zhang, J.; Lei, S. L.; Yan, M.; Xie, W. T.; Qi, X. Y.; Wang, H. J.; Xiao, J. M.; Chen, S. Y.; Li, S. J. et al. Atomically precise multi-domain $Gd_xFe_{3-x}O_4$ nanoclusters with modulated contrast properties for T_2-weighted magnetic resonance imaging of early orthotopic cancer. *Chem. Eng. J.* **2022**, *429*, 132255.

[36] Liang, Z. Y.; Xie, S. Z.; Wang, Q. Y.; Zhang, B.; Xiao, L.; Wang, C. H.; Liu, X.; Chen, Y.; Yang, S. F.; Du, H. et al. Ligand-induced atomically segregation-tunable alloy nanoprobes for enhanced magnetic resonance imaging. *ACS Nano* **2024**, *18*, 15249–15260.

[37] Liang, Z. Y.; Xiao, L.; Wang, Q. Y.; Zhang, B.; Mo, W. K.; Xie, S. Z.; Liu, X.; Chen, Y.; Yang, S. F.; Du, H. et al. Ligand-mediated magnetism-conversion nanoprobes for activatable ultra-high field magnetic resonance imaging. *Angew. Chem., Int. Ed.* **2024**, *63*, e202318948.

[38] Salafranca, J.; Gazquez, J.; Pérez, N.; Labarta, A.; Pantelides, S. T.; Pennycook, S. J.; Batlle, X.; Varela, M. Surfactant organic molecules restore magnetism in metal-oxide nanoparticle surfaces. *Nano Lett.* **2012**, *12*, 2499–2503.

[39] Laha, S. S.; Thorat, N. D.; Singh, G.; Sathish, C. I.; Yi, J. B.; Dixit, A.; Vinu, A. Rare-earth doped iron oxide nanostructures for cancer theranostics: Magnetic hyperthermia and magnetic resonance imaging. *Small* **2022**, *18*, 2104855.

[40] Miao, Y. Q.; Zhang, H.; Cai, J.; Chen, Y. M.; Ma, H. J.; Zhang, S.; Yi, J. B.; Liu, X. L.; Bay, B. H.; Guo, Y. K. et al. Structure-relaxivity mechanism of an ultrasmall ferrite nanoparticle T_1 MR contrast agent: The impact of dopants controlled crystalline core and surface disordered shell. *Nano Lett.* **2021**, *21*, 1115–1123.

[41] Li, R. Z.; Zhao, J.; Liu, B. Z.; Wang, D. S. Atomic distance engineering in metal catalysts to regulate catalytic performance. *Adv. Mater.* **2024**, *36*, 2308653.

[42] Hens, Z.; De Roo, J. Atomically precise nanocrystals. *J. Am. Chem. Soc.* **2020**, *142*, 15627–15637.

[43] Fang, H. Y.; Mahalingam, H.; Li, X. Z.; Han, X.; Qiu, Z. Z.; Han, Y. X.; Noori, K.; Dulal, D.; Chen, H. F.; Lyu, P. et al. Atomically precise vacancy-assembled quantum antidots. *Nat. Nanotechnol.* **2023**, *18*, 1401–1408.

[44] Yao, C. H.; Guo, N.; Xi, S. B.; Xu, C. Q.; Liu, W.; Zhao, X. X.; Li, J.; Fang, H. Y.; Su, J.; Chen, Z. X. et al. Atomically-precise dopant-controlled single cluster catalysis for electrochemical nitrogen reduction. *Nat. Commun.* **2020**, *11*, 4389.

[45] Hou, Z. Q.; Cui, C. H.; Li, Y. N.; Gao, Y. J.; Zhu, D. M.; Gu, Y. F.; Pan, G. Y.; Zhu, Y. Q.; Zhang, T. Lattice-strain engineering for heterogenous electrocatalytic oxygen evolution reaction. *Adv. Mater.* **2023**, *35*, 2209876.

[46] Choi, J. S.; Kim, S.; Yoo, D.; Shin, T. H.; Kim, H.; Gomes, M. D.; Kim, S. H.; Pines, A.; Cheon, J. Distance-dependent magnetic resonance tuning as a versatile MRI sensing platform for biological targets. *Nat. Mater.* **2017**, *16*, 537–542.

[47] Du, H.; Wang, Q. Y.; Liang, Z. Y.; Li, Q. L.; Li, F. Y.; Ling, D. S. Fabrication of magnetic nanoprobes for ultrahigh-field magnetic resonance imaging. *Nanoscale* **2022**, *14*, 17483–17499.

[48] Du, H.; Wang, Q. Y.; Zhang, B.; Liang, Z. Y.; Huang, C. Y.; Shi, D.; Li, F. Y.; Ling, D. S. Structural defect-enabled magnetic neutrality nanoprobes for ultra-high-field magnetic resonance imaging of isolated tumor cells *in vivo*. *Adv. Mater.* **2024**, *36*, 2401538.

[49] Guan, G. Q.; Zhang, C.; Liu, H. Y.; Wang, Y. J.; Dong, Z.; Lu, C.; Nan, B.; Yue, R. Y.; Yin, X.; Zhang, X. B. et al. Ternary alloy PtWMn as a Mn nanoreservoir for high-field MRI monitoring and highly selective ferroptosis therapy. *Angew. Chem., Int. Ed.* **2022**, *61*, e202117229.

[50] Liu, H. J.; Jiang, Y.; Li, Q. Q.; Hai, G. T.; Gu, C.; Du, Y. P. Interface-triggered spin-magnetic effect in rare earth intraparticle heterostructured nanoalloys for boosting hydrogen evolution. *Angew. Chem., Int. Ed.* **2024**, *63*, e202412591.

[51] Yu, M.; Li, S. M.; Ren, X. L.; Liu, N.; Guo, W. N.; Xue, J.; Tan, L. F.; Fu, C. H.; Wu, Q.; Niu, M. et al. Magnetic bimetallic heterointerface nanomissiles with enhanced microwave absorption for microwave thermal/dynamics therapy of breast cancer. *ACS Nano* **2024**, *18*, 3636–3650.

[52] Seo, W. S.; Lee, J. H.; Sun, X. M.; Suzuki, Y.; Mann, D.; Liu, Z.; Terashima, M.; Yang, P. C.; McConnell, M. V.; Nishimura, D. G. et al. FeCo/graphitic-shell nanocrystals as advanced magnetic-resonance-imaging and near-infrared agents. *Nat. Mater.* **2006**, *5*, 971–976.

[53] Liang, Z. Y.; Wang, Q. Y.; Liao, H. W.; Zhao, M.; Lee, J.; Yang, C.; Li, F. Y.; Ling, D. S. Artificially engineered antiferromagnetic nanoprobes for ultra-sensitive histopathological level magnetic resonance imaging. *Nat. Commun.* **2021**, *12*, 3840.

[54] Zhang, T. T.; Wang, Z. J.; Xiang, H. J.; Xu, X.; Zou, J.; Lu, C. C. Biocompatible superparamagnetic europium-doped iron oxide nanoparticle clusters as multifunctional nanoprobes for multimodal *in vivo* imaging. *ACS Appl. Mater. Interfaces* **2021**, *13*, 33850–33861.

[55] Fernández-Barahona, I.; Gutiérrez, L.; Veintemillas-Verdaguer, S.; Pellico, J.; del Puerto Morales, M.; Catala, M.; del Pozo, M. A.; Ruiz-

Cabello, J.; Herranz, F. Cu-doped extremely small iron oxide nanoparticles with large longitudinal relaxivity: One-pot synthesis and *in vivo* targeted molecular imaging. *ACS Omega* **2019**, *4*, 2719–2727.

[56] Ma, Y. Y.; Xia, J. B.; Yao, C. Y.; Yang, F.; Stanciu, S. G.; Li, P.; Jin, Y. H.; Chen, T. X.; Zheng, J. J.; Chen, G. P. et al. Precisely tuning the contrast properties of $Zn_xFe_{3-x}O_4$ nanoparticles in magnetic resonance imaging by controlling their doping content and size. *Chem. Mater.* **2019**, *31*, 7255–7264.

[57] Lee, J. H.; Huh, Y. M.; Jun, Y. W.; Seo, J. W.; Jang, J. T.; Song, H. T.; Kim, S.; Cho, E. J.; Yoon, H. G.; Suh, J. S. et al. Artificially engineered magnetic nanoparticles for ultra-sensitive molecular imaging. *Nat. Med.* **2007**, *13*, 95–99.

[58] Shin, T. H.; Kang, S.; Park, S.; Choi, J. S.; Kim, P. K.; Cheon, J. A magnetic resonance tuning sensor for the MRI detection of biological targets. *Nat. Protoc.* **2018**, *13*, 2664–2684.

[59] Gao, J. H.; Wang, Y.; Meng, X. F.; Wang, X. S.; Han, F.; Xing, H.; Lv, G. L.; Zhang, L.; Wu, S. M.; Jiang, X. W. et al. A FAPα-activated MRI nanoprobe for precise grading diagnosis of clinical liver fibrosis. *Nat. Commun.* **2024**, *15*, 8036.

[60] Dai, J. D.; Liu, Z.; Wang, L. L.; Huang, G. M.; Song, S. J.; Chen, C.; Wu, T.; Xu, X.; Hao, C. J.; Bian, Y. J. et al. A telomerase-activated magnetic resonance imaging probe for consecutively monitoring tumor growth kinetics and *in situ* screening inhibitors. *J. Am. Chem. Soc.* **2023**, *145*, 1108–1117.

[61] Wang, Z. L.; Xue, X. D.; Lu, H. W.; He, Y. X.; Lu, Z. W.; Chen, Z. J.; Yuan, Y.; Tang, N.; Dreyer, C. A.; Quigley, L. et al. Two-way magnetic resonance tuning and enhanced subtraction imaging for non-invasive and quantitative biological imaging. *Nat. Nanotechnol.* **2020**, *15*, 482–490.

[62] Liu, J. P.; Li, L.; Zhang, R.; Ping Xu, Z. P. The adjacent effect between Gd(III) and Cu(II) in layered double hydroxide nanoparticles synergistically enhances T_1-weighted magnetic resonance imaging contrast. *Nanoscale Horiz.* **2023**, *8*, 279–290.

[63] Matus, M. F.; Häkkinen, H. Understanding ligand-protected noble metal nanoclusters at work. *Nat. Rev. Mater.* **2023**, *8*, 372–389.

[64] Hassan, Y.; Park, J. H.; Crawford, M. L.; Sadhanala, A.; Lee, J.; Sadighian, J. C.; Mosconi, E.; Shivanna, R.; Radicchi, E.; Jeong, M. et al. Ligand-engineered bandgap stability in mixed-halide perovskite LEDs. *Nature* **2021**, *591*, 72–77.

[65] Liu, P. X.; Qin, R. X.; Fu, G.; Zheng, N. F. Surface coordination chemistry of metal nanomaterials. *J. Am. Chem. Soc.* **2017**, *139*, 2122–2131.

[66] Boles, M. A.; Ling, D. S.; Hyeon, T.; Talapin, D. V. The surface science of nanocrystals. *Nat. Mater.* **2016**, *15*, 141–153.

[67] Bhattacharjee, K.; Prasad, B. L. V. Surface functionalization of inorganic nanoparticles with ligands: A necessary step for their utility. *Chem. Soc. Rev.* **2023**, *52*, 2573–2595.

[68] Wang, W. T.; Mattoussi, H. Engineering the bio-nano interface using a multifunctional coordinating polymer coating. *Acc. Chem. Res.* **2020**, *53*, 1124–1138.

[69] Lin, G. Y.; Zhang, M. Q. Ligand chemistry in antitumor theranostic nanoparticles. *Acc. Chem. Res.* **2023**, *56*, 1578–1590.

[70] Heuer-Jungemann, A.; Feliu, N.; Bakaimi, I.; Hamaly, M.; Alkilany, A.; Chakraborty, I.; Masood, A.; Casula, M. F.; Kostopoulou, A.; Oh, E. et al. The role of ligands in the chemical synthesis and applications of inorganic nanoparticles. *Chem. Rev.* **2019**, *119*, 4819–4880.

[71] Calvin, J. J.; Brewer, A. S.; Alivisatos, A. P. The role of organic ligand shell structures in colloidal nanocrystal synthesis. *Nat. Synth.* **2022**, *1*, 127–137.

[72] Parkinson, G. S.; Mulakaluri, N.; Losovyj, Y.; Jacobson, P.; Pentcheva, R.; Diebold, U. Semiconductor-half metal transition at the Fe_3O_4 (001) surface upon hydrogen adsorption. *Phys. Rev. B* **2010**, *82*, 125413.

[73] Kurahashi, M.; Sun, X.; Yamauchi, Y. Recovery of the half-metallicity of an Fe_3O_4 (100) surface by atomic hydrogen adsorption. *Phys. Rev. B* **2010**, *81*, 193402.

[74] Wang, C.; Sun, W. B.; Zhang, J.; Zhang, J. P.; Guo, Q. H.; Zhou, X. Y.; Fan, D. D.; Liu, H. R.; Qi, M.; Gao, X. H. et al. An electric-field-responsive paramagnetic contrast agent enhances the visualization of epileptic foci in mouse models of drug-resistant epilepsy. *Nat. Biomed. Eng.* **2021**, *5*, 278–289.

[75] Yao, J. T.; Yang, Z. W.; Huang, L. D.; Yang, C.; Wang, J. X.; Cao, Y.; Hao, L.; Zhang, L.; Zhang, J. Q.; Li, P. et al. Low-intensity focused ultrasound-responsive ferrite-encapsulated nanoparticles for atherosclerotic plaque neovascularization theranostics. *Adv. Sci.* **2021**, *8*, 2100850.

[76] Wen, L. Y.; Fu, X. M.; Zhang, H.; Ye, P. F.; Fu, H.; Zhou, Z. Q.; Sun, R.; Xu, T.; Fu, C.; Zhu, C. C. et al. Tailoring zinc ferrite nanoparticle surface coating for macrophage-affinity magnetic resonance imaging of atherosclerosis. *ACS Appl. Mater. Interfaces* **2024**, *16*, 13496–13508.

[77] Montiel Schneider, M. G.; Martín, M. J.; Otarola, J.; Vakarelska, E.; Simeonov, V.; Lassalle, V.; Nedyalkova, M. Biomedical applications of iron oxide nanoparticles: Current insights progress and perspectives. *Pharmaceutics* **2022**, *14*, 204.

[78] Wong, X. Y.; Sena-Torralba, A.; Álvarez-Diduk, R.; Muthoosamy, K.; Merkoçi, A. Nanomaterials for nanotheranostics: Tuning their properties according to disease needs. *ACS Nano* **2020**, *14*, 2585–2627.

[79] Zeng, W. W.; Wu, Z. Y.; Xu, Y.; Yang, W. T.; Zhang, B. B. Furin-catalyzed enhanced magnetic resonance imaging probe for differential diagnosis of malignant breast cancers. *Anal. Chem.* **2024**, *96*, 6707–6714.

[80] Yue, R. Y.; Li, Z.; Liu, H. Y.; Wang, Y. J.; Li, Y. H.; Yin, R.; Yin, B. L.; Qian, H. S.; Kang, H.; Zhang, X. B. et al. Imaging-guided companion diagnostics in radiotherapy by monitoring APE1 activity with afterglow and MRI imaging. *Nat. Commun.* **2024**, *15*, 6349.

[81] Maas, M. B.; Lev, M. H.; Ay, H.; Singhal, A. B.; Greer, D. M.; Smith, W. S.; Harris, G. J.; Halpern, E.; Kemmling, A.; Koroshetz, W. J. et al. Collateral vessels on CT angiography predict outcome in acute ischemic stroke. *Stroke* **2009**, *40*, 3001–3005.

[82] Liebeskind, D. S.; Tomsick, T. A.; Foster, L. D.; Yeatts, S. D.; Carrozzella, J.; Demchuk, A. M.; Jovin, T. G.; Khatri, P.; von Kummer, R.; Sugg, R. M. et al. Collaterals at angiography and outcomes in the interventional management of stroke (IMS) III trial. *Stroke* **2014**, *45*, 759–764.

[83] Shin, T. H.; Kim, P. K.; Kang, S.; Cheong, J.; Kim, S.; Lim, Y.; Shin, W.; Jung, J. Y.; Lah, J. D.; Choi, B. W. et al. High-resolution T_1 MRI via renally clearable dextran nanoparticles with an iron oxide shell. *Nat. Biomed. Eng.* **2021**, *5*, 252–263.

[84] Zhang, P. S.; Cheng, J. W.; Lu, Y. J.; Zhang, N.; Wu, X. A.; Lin, H.; Li, W.; Wang, J.; Winnik, M. A.; Gan, Z. H. et al. Hypersensitive MR angiography based on interlocking stratagem for diagnosis of cardiac-cerebral vascular diseases. *Nat. Commun.* **2023**, *14*, 6149.

[85] Li, W. Y.; Zhang, R. R.; Zhang, X. Y.; Wu, S.; Ma, T. C.; Hou, Y.; Zeng, J. F.; Gao, M. Y. Precise diagnosis of cardiac-cerebral vascular diseases with magnetic resonance imaging-based nanoprobes. *iRADIOLOGY* **2024**, *2*, 264–284.

[86] Jolly, S. S.; Yusuf, S.; Cairns, J.; Niemelä, K.; Xavier, D.; Widimsky, P.; Budaj, A.; Niemelä, M.; Valentin, V.; Lewis, B. S. et al. Radial versus femoral access for coronary angiography and intervention in patients with acute coronary syndromes (RIVAL): A randomised, parallel group, multicentre trial. *Lancet* **2011**, *377*, 1409–1420.

[87] Ran, Y. C.; Wang, Y. T.; Zhu, M.; Wu, X.; Malhotra, A.; Lei, X. W.; Zhang, F. F.; Wang, X.; Xie, S. S.; Zhou, J. et al. Higher plaque burden of middle cerebral artery is associated with recurrent ischemic stroke. *Stroke* **2020**, *51*, 659–662.

[88] Dirnagl, U.; Iadecola, C.; Moskowitz, M. A. Pathobiology of

ischaemic stroke: An integrated view. *Trends Neurosci.* **1999**, *22*, 391–397.
[89] Ouriel, K. Peripheral arterial disease. *Lancet* **2001**, *358*, 1257–1264.
[90] Reinecke, H.; Unrath, M.; Freisinger, E.; Bunzemeier, H.; Meyborg, M.; Luders, F.; Gebauer, K.; Roeder, N.; Berger, K.; Malyar, N. M. Peripheral arterial disease and critical limb ischaemia: Still poor outcomes and lack of guideline adherence. *Eur. Heart J.* **2015**, *36*, 932–938.
[91] Wilcox, N. S.; Amit, U.; Reibel, J. B.; Berlin, E.; Howell, K.; Ky, B. Cardiovascular disease and cancer: Shared risk factors and mechanisms. *Nat. Rev. Cardiol.* **2024**, *21*, 617–631.
[92] Galli, M.; Niccoli, G.; De Maria, G.; Brugaletta, S.; Montone, R. A.; Vergallo, R.; Benenati, S.; Magnani, G.; D'Amario, D.; Porto, I. et al. Coronary microvascular obstruction and dysfunction in patients with acute myocardial infarction. *Nat. Rev. Cardiol.* **2024**, *21*, 283–298.
[93] GBD 2017 US Neurological Disorders Collaborators. Burden of neurological disorders across the US from 1990-2017: A global burden of disease study. *JAMA Neurol.* **2021**, *78*, 165–176.
[94] GBD 2021 Nervous System Disorders Collaborators. Global, regional, and national burden of disorders affecting the nervous system, 1990-2021: A systematic analysis for the global burden of disease study 2021. *Lancet Neurol.* **2024**, *23*, 344–381.
[95] Mahammedi, A.; Saba, L.; Vagal, A.; Leali, M.; Rossi, A.; Gaskill, M.; Sengupta, S.; Zhang, B.; Carriero, A.; Bachir, S. et al. Imaging of neurologic disease in hospitalized patients with COVID-19: An Italian multicenter retrospective observational study. *Radiology* **2020**, *297*, E270–E273.
[96] Politis, M.; Piccini, P. Positron emission tomography imaging in neurological disorders. *J. Neurol.* **2012**, *259*, 1769–1780.
[97] Wu, Z. Y.; Yang, W. T.; Zhang, B. B. Enzyme-catalyzed molecular MR imaging of tumors. *TrAC Trends Anal. Chem.* **2024**, *178*, 117848.
[98] Zhao, Y. J.; Ding, Y.; Lau, V.; Man, C.; Su, S.; Xiao, L. F.; Leong, A. T. L.; Wu, E. X. Whole-body magnetic resonance imaging at 0.05 tesla. *Science* **2024**, *384*, eadm7168.
[99] Zhang, J. Y.; Yu, L. D.; Yu, M. H.; Yu, D. H.; Chen, Y.; Zhang, J. Engineering nanoprobes for magnetic resonance imaging of brain diseases. *Chem. Eng. J.* **2024**, *481*, 148472.
[100] Chen, Y.; Liang, Z. Y.; Wang, Q. Y.; Xiao, L.; Xie, S. Z.; Yang, S. F.; Liu, X.; Ling, D. S.; Li, F. Y. Alpha-synuclein oligomers driven T_1-T_2 switchable nanoprobes for early and accurate diagnosis of parkinson's disease. *Adv. Mater.* **2024**, *36*, 2310404.
[101] Liu, J. M.; Chen, C. Y.; Chen, H. T.; Huang, C.; Ren, Q. F.; Sun, M. Y.; Tao, J.; Lin, B. Q.; Zhao, P. Brain glucose activated MRI contrast agent for early diagnosis of Alzheimer's disease. *Anal. Chem.* **2022**, *94*, 16213–16221.
[102] Wang, Q. Y.; Wang, T.; Yang, S. F.; Du, H.; Zhang, B.; Cui, S. R.; Ling, D. S.; Li, F. Y. Highly sensitive diagnosis of extracellular calcium ions associated brain diseases using Ca^{2+}-dependent T_2-T_1 switchable magnetic nanosensors. *Adv. Funct. Mater.* **2024**, *34*, 2313286.
[103] Qian, J.; Yang, Z. C.; Lyu, J. K.; Yao, Q. F.; Xie, J. P. Molecular interactions in atomically precise metal nanoclusters. *Precis. Chem.* **2024**, *2*, 495–517.
[104] Pollice, R.; dos Passos Gomes, G.; Aldeghi, M.; Hickman, R. J.; Krenn, M.; Lavigne, C.; Lindner-D'Addario, M.; Nigam, A.; Ser, C. T.; Yao, Z. et al. Data-driven strategies for accelerated materials design. *Acc. Chem. Res.* **2021**, *54*, 849–860.
[105] Tao, H. C.; Wu, T. Y.; Aldeghi, M.; Wu, T. C.; Aspuru-Guzik, A.; Kumacheva, E. Nanoparticle synthesis assisted by machine learning. *Nat. Rev. Mater.* **2021**, *6*, 701–716.
[106] Jordan, M. I.; Mitchell, T. M. Machine learning: Trends, perspectives, and prospects. *Science* **2015**, *349*, 255–260.
[107] Butler, K. T.; Davies, D. W.; Cartwright, H.; Isayev, O.; Walsh, A. Machine learning for molecular and materials science. *Nature* **2018**, *559*, 547–555.
[108] Yang, L.; Wang, H.; Leng, D. Y.; Fang, S. P.; Yang, Y. N.; Du, Y. R. Machine learning applications in nanomaterials: Recent advances and future perspectives. *Chem. Eng. J.* **2024**, *500*, 156687.
[109] Benavides-Hernández, J.; Dumeignil, F. From characterization to discovery: Artificial intelligence, machine learning and high-throughput experiments for heterogeneous catalyst design. *ACS Catal.* **2024**, *14*, 11749–11779.
[110] Hsu, J. C.; Tang, Z. M.; Eremina, O. E.; Sofias, A. M.; Lammers, T.; Lovell, J. F.; Zavaleta, C.; Cai, W. B.; Cormode, D. P. Nanomaterial-based contrast agents. *Nat. Rev. Methods Primer* **2023**, *3*, 30.
[111] Leong, H. S.; Butler, K. S.; Brinker, C. J.; Azzawi, M.; Conlan, S.; Dufés, C.; Owen, A.; Rannard, S.; Scott, C.; Chen, C. Y. et al. On the issue of transparency and reproducibility in nanomedicine. *Nat. Nanotechnol.* **2019**, *14*, 629–635.
[112] Gavilán, H.; Rizzo, G. M. R.; Silvestri, N.; Mai, B. T.; Pellegrino, T. Scale-up approach for the preparation of magnetic ferrite nanocubes and other shapes with benchmark performance for magnetic hyperthermia applications. *Nat. Protoc.* **2023**, *18*, 783–809.
[113] Park, W.; Shin, H.; Choi, B.; Rhim, W. K.; Na, K.; Keun Han, D. Advanced hybrid nanomaterials for biomedical applications. *Prog. Mater. Sci.* **2020**, *114*, 100686.
[114] Deng, X. J.; Wang, J. H.; Yu, S. S.; Tan, S. Y.; Yu, T. T.; Xu, Q. X.; Chen, N. H.; Zhang, S. Q.; Zhang, M. R.; Hu, K. et al. Advances in the treatment of atherosclerosis with ligand-modified nanocarriers. *Exploration* **2024**, *4*, 20230090.